The impact of variable sea ice roughness on changes in Arctic Ocean surface stress: a model study

Article

Published Version

www.reading.ac.uk/centaur

CentAUR

Central Archive at the University of Reading

Reading's research outputs online

The impact of variable sea ice roughness on changes in Arctic Ocean surface stress: A model study

Torge Martin[1], Michel Tsamados[2,3], David Schroeder[2], and Daniel L. Feltham[2]

[1]GEOMAR Helmholtz Centre for Ocean Research Kiel, Kiel, Germany, [2]Centre for Polar Observation and Modelling, Department of Meteorology, University of Reading, Reading, UK, [3]Now at Centre for Polar Observation and Modelling, Department of Earth Sciences, University College London, London, UK

Abstract The Arctic sea ice cover is thinning and retreating, causing changes in surface roughness that in turn modify the momentum flux from the atmosphere through the ice into the ocean. New model simulations comprising variable sea ice drag coefficients for both the air and water interface demonstrate that the heterogeneity in sea ice surface roughness significantly impacts the spatial distribution and trends of ocean surface stress during the last decades. Simulations with constant sea ice drag coefficients as used in most climate models show an increase in annual mean ocean surface stress (0.003 N/m^2 per decade, 4.6%) due to the reduction of ice thickness leading to a weakening of the ice and accelerated ice drift. In contrast, with variable drag coefficients our simulations show annual mean ocean surface stress is declining at a rate of -0.002 N/m^2 per decade (3.1%) over the period 1980–2013 because of a significant reduction in surface roughness associated with an increasingly thinner and younger sea ice cover. The effectiveness of sea ice in transferring momentum does not only depend on its resistive strength against the wind forcing but is also set by its top and bottom surface roughness varying with ice types and ice conditions. This reveals the need to account for sea ice surface roughness variations in climate simulations in order to correctly represent the implications of sea ice loss under global warming.

1. Introduction

Wind exerts a stress on the ocean surface thereby driving currents. In polar regions sea ice moderates this momentum flux, altering the ocean forcing, while being itself forced by both wind and currents. The surface stress increases with increasing surface roughness. Open water surface roughness is of transient character as wind waves decay when the wind relaxes. Sea ice roughness formed by obstacles such as pressure ridges and floe edges at both surfaces, top and underside of the ice, can accumulate and last over a season. Sea ice surface roughness is thus related to the mean ice thickness.

Arctic sea ice thinning [*Lindsay and Schweiger*, 2015], retreat [*Cavalieri and Parkinson*, 2012], and the extensive loss of multiyear ice during the late 1990s and early 2000s [*Maslanik et al.*, 2011] suggest that the surface characteristics of the Arctic sea ice cover have changed with consequences for both air-ice and ice-water drag. Airborne observations of sea ice freeboard, ridge height and spacing from various locations around the Arctic show significant variability of sea ice surface roughness and also reveal large-scale spatial patterns [*Martin*, 2007; *Castellani et al.*, 2014] but the temporal evolution is rather unclear. Here sea ice roughness is used as a general term to describe the potential of sea ice structures, such as pressure ridges and floe edges characterized by their average height and spacing, to act as obstacles to the surface wind and currents, thus enhancing friction and momentum exchange with the ice. Surface roughness is increased by, for instance, deformation in convergent ice motion and break up by waves but is decreased by refreezing and formation of new ice. In this respect an ice cover consisting of flat but thick floes with open water in between can be similarly rough as a closed ridged ice cover.

The recent model study by *Tsamados et al.* [2014] provides a first idea of how sea ice roughness and drag coefficients may have evolved over the past decades: Surface roughness decreased along the coasts of Greenland, Canada, and Alaska year-round and in summers also in the eastern Arctic (Transpolar Drift Stream) from 1990 to 2012. In contrast, ice roughness increased during this period in the Chukchi Sea in winter and in the central Canada Basin more in summer than in winter. Large-scale changes in surface

roughness may impact ocean and sea ice transports by moderating the effectiveness of the wind forcing. So far, sea ice roughness has not been taken into account in explanations of trends in, for instance, Fram Strait sea ice export [e.g., *Kwok et al.*, 2013], coastal upwelling and off-shore downwelling [*Yang*, 2009], the recent spin up of the Beaufort Gyre [*Giles et al.*, 2012; *McPhee*, 2013] and a growing freshwater storage [*McPhee et al.*, 2009; *Rabe et al.*, 2011]. We thus need to better understand how changes in sea ice roughness affect the dynamics of the ice cover and the ocean underneath.

How do changing sea ice characteristics affect the momentum flux into the Arctic Ocean? The common notion is that sea ice shields the ocean from interaction with the atmosphere damping heat, mass and momentum fluxes. Since the Arctic sea ice cover is shrinking this implies an increasing momentum flux into the ocean. Even more, completely ice-free areas in the Arctic in summers could be stirred by strong winds directly as indicated by mooring observations [*Rainville and Woodgate*, 2009; *Martini et al.*, 2014]. Indeed a thinner and thus weaker sea ice cover is more susceptible to the wind forcing, drifts faster, and transfers more momentum into the ocean underneath according to a recent study with the Polar Science Center's coupled sea ice and ocean model PIOMAS [*Martin et al.*, 2014]. This leads to a positive trend in ocean surface stress on annual mean and in particular during the long winter season. The authors also pointed out that sea ice has the potential to amplify momentum transfer into the ocean when in free drift compared to the direct air-sea flux. This is the case when the sea ice surface is rougher than the surface of open water and ocean surface layer stability does not hinder the exchange of momentum. *Martin et al.* [2014] suggest that such amplification of momentum transfer by ice floes peaks at an optimal ice concentration of 80–90% as overall surface roughness increases with increasing ice concentration but momentum transfer is damped by internal ice stresses at even higher concentrations. Naturally, this amplification potential of sea ice depends on the contrast between open water and sea ice roughness. While observations generally support a difference in surface roughness between open water and sea ice they also show that assuming just a constant ice roughness in models is too simple [e.g., *Guest and Davidson*, 1991].

Assuming the wind at 10 m height as the ultimate source of momentum, the momentum transfer from the atmosphere to sea ice and ocean depends on atmospheric surface layer stability, ocean surface stratification, surface roughness at the interface, and sea ice internal stresses. We focus on the latter two factors. In particular, we use the Los Alamos sea ice model CICE [*Hunke et al.*, 2013] to simulate how spatial and temporal variability of both air-ice and ice-water surface roughness as well as ice internal forces affect the momentum transfer. In our analysis we will use the expression "surface roughness" synonymously for the total neutral drag coefficient. We take an oceanic perspective throughout the manuscript and study the surface stress acting on the ocean with the associated open water and ice-water drag coefficients. As can be seen from the complete set of model-specific surface stress and neutral drag coefficient equations provided in Appendix A air-ice and ice-water drag (i.e., surface or interface roughness) are treated in an analogous manner.

In ice-covered seas the total ocean surface stress τ_{ocn} is commonly computed as the sum of the surface air stress on open water τ_{ao} and the ice-water stress τ_{iw} weighted by the ice-covered area fraction, a.k.a. sea ice concentration A_i:

$$\vec{\tau}_{ocn} = (1 - A_i)\vec{\tau}_{ao} + A_i\vec{\tau}_{iw} \tag{1}$$

The individual surface stresses can be estimated from the near-surface velocities by a quadratic drag law:

$$\vec{\tau}_{ao} = \rho_a C_{dao}|\vec{u}_a - \vec{u}_w|(\vec{u}_a - \vec{u}_w) \tag{2a}$$

$$\vec{\tau}_{iw} = \rho_w C_{dw}\ |\vec{u}_i - \vec{u}_w|(\vec{u}_i - \vec{u}_w) \tag{2b}$$

where ρ_a and ρ_w are the densities of air and water, and C_{dao} and C_{dw} denote the atmospheric drag coefficient at the open water surface and the oceanic drag coefficient at the ice-water interface. The wind velocity $\boldsymbol{u}_a$ is typically provided at 10 m height. Ocean currents $\boldsymbol{u}_w$ are often neglected from the open water surface stress balance (equation (2a)) assuming that $|\boldsymbol{u}_a| \gg |\boldsymbol{u}_w|$; they are taken from the uppermost level that can be assumed to be undisturbed by surface processes to determine the relative ice drift velocity $\boldsymbol{u}_i$ for the under ice surface stress (equation (2b)). The drag coefficients are functions of the surface roughness length and stability of near-surface stratification. While this is accounted for with respect to the air-ice drag coefficient in CICE and some other large-scale sea ice-ocean models by applying an atmospheric surface layer model

[see *Briegleb et al.*, 2004], similar approaches for the interface with the ocean [e.g., *McPhee*, 2012] have not yet been implemented. Over open water the atmospheric drag coefficient is often parameterized as a function of wind speed in ocean models following *Large and Pond* [1981]

$$C_{dao} = (2.7|\vec{u}_a|^{-1} + 0.142 + 0.0764|\vec{u}_a|)10^{-3} \; . \tag{3}$$

This empirical relationship accounts for higher drag at very low wind speeds due to small scale turbulence under calm conditions and for increasing surface roughness with increasing wind speed above ∼3 m/s related to the formation of wind waves. In contrast, many sea ice models, including PIOMAS used by *Martin et al.* [2014], only apply a constant value for the ice roughness length or drag coefficient.

Recently, *Tsamados et al.* [2014] implemented variable sea-ice drag coefficients into the sea ice model CICE, which allows to distinguish between skin drag (C_{dw_skin}) and form drag in basin-scale simulations similar to *Steiner et al.* [1999]. However, Steiner et al. only considered form drag by pressure ridges whereas *Tsamados et al.* [2014] derived separate equations for form drag coefficients from ridges (C_{dw_ridge}) as well as floe edges (C_{dw_floe}) at both the air-ice (subscript *a*) and ice-water interface (subscript *w*) and—inspired by earlier studies [e.g., *Andreas et al.*, 2010; *Lüpkes et al.*, 2012]—melt pond edges at the air-ice interface only. The sum of the individual drag coefficients then yields the total ice-water drag coefficient

$$C_{dw} = C_{dw\_skin} + C_{dw\_ridge} + C_{dw\_floe} \; . \tag{4}$$

In this new parameterization the drag coefficients are dynamically coupled to the sea ice topography and can evolve in space and time.

Tsamados et al. [2014] show for the summer season that floe edges dominate the total ice-water drag coefficient magnitude and its trend over the past two decades. This hints at the possibility that a favorable decrease in floe size associated with decreasing ice concentration yields higher form drag at ice concentrations lower than 80% not accounted for in the model of *Martin et al.* [2014]. Then this effect has the potential to offset the decline in ocean surface stress caused by growing open water fractions of reduced surface roughness on the regional scale.

Here we investigate the impact of explicitly simulating variable drag coefficients, altered by dynamically derived parameters of pressure ridges, melt ponds, and ice floes, on the spatial distribution of ocean surface stress in the Arctic, its trends since 1980, and the concept of an optimal ice concentration for momentum transfer. In particular, we will address the following two questions: Does decreasing ice strength or decreasing surface roughness—both associated with sea ice thinning but with opposing consequences for momentum transfer—have a greater impact on ocean surface stress? And can floe edges increase surface roughness so that sea ice area loss does not necessarily mean ocean surface stress decline in summer?

The manuscript is structured as follows: section 2 provides a brief overview of the numerical model on which our study is based. Results are then presented in section 3 in which we first discuss the general effect of variable versus constant drag coefficients on ocean surface stress, then look in detail at the role of dominant factors in the winter and summer season, study the relationship of ocean surface stress to ice concentration and thickness, and finally address the potential of sea ice to damp or enhance momentum transfer. A discussion in section 4 compares our results with previous studies and sheds light on potential caveats of our method before we summarize our conclusions in section 5.

2. Methods

2.1. Model Set Up

The Los Alamos sea ice model CICE (version 5.0.4) [*Hunke et al.*, 2013] is run in stand-alone mode on a tripolar grid that covers a pan-Arctic region with a horizontal grid resolution of around 40 km. Our default setup is the same as in *Tsamados et al.* [2014] apart from using a more recent model version including updates described in detail in *Tsamados et al.* [2015]. Most notably, we calculate the neutral sensible heat transfer coefficient as a function of the neutral ice-water drag coefficient $\alpha_h = C_{dw}/2$. The model is forced by atmospheric fields of the NCEP-DOE-2 reanalysis [*Kanamitsu et al.*, 2002]: 6 hourly 10 m winds, 2 m temperatures and 2 m humidity, and daily shortwave and longwave radiation, as well as monthly mean snowfall and precipitation rates. Sea surface salinity and ocean currents (at a depth of 3 m) are prescribed from

climatological monthly means derived from the MYO-WP4-PUM-GLOBAL-REANALYSIS-PHYS-001-004 (MYO) reanalysis [*Ferry et al.*, 2011]. Sea surface temperature is computed as a prognostic variable from fluxes but initialized from the MYO reanalysis. Starting with an isotropic homogeneous sea ice cover of 2.5 m thickness and 100% concentration as well as a snow depth of 20 cm the model is spun up for 17 years (1979–1995) once. This configuration is used as initial condition for all the numerical experiments discussed in the following running from 1979 to 2013. In the analysis we skip 1979 because the first year is influenced by the restart of the model from 1995 conditions.

We run a baseline experiment with variable drag coefficients (FORM) resembling the main experiment of *Tsamados et al.* [2014]. We use the same choice of parameters determining the variable neutral drag coefficients for both the air-ice and the ice-water interface that were shown to produce a realistic range of values of total neutral drag coefficients, while also maintaining realistic average values for the ridge sail and keel height and frequency. For comparison, we also perform a reference simulation SKIN with constant total neutral drag coefficients for the air-ice and the ice-water interface $C_{da} = 1.3 \times 10^{-3}$ and $C_{dw} = 5.8 \times 10^{-3}$. These values equal the Arctic long-term mean total neutral drag coefficients of FORM. In all simulations, effects of atmospheric surface layer stability are accounted for in the total air-ice drag coefficient, which enters the surface stress computation, by applying the model described in *Briegleb et al.* [2004].

In order to test the robustness of our results and in particular the sensitivity of ocean surface stress on the floe edge form drag parameterization (see Appendix A, equation (A5)) we conduct two additional experiments in which the floe size distribution parameter β is changed from 0.5 used in FORM to 0.3 (FORM_beta03) and 1.4 (FORM_beta14), which are the lower and upper bounds suggested by *Lüpkes et al.* [2012] for the calculation of the floe length L_f:

$$L_f = L_{min} \left(\frac{A_\star}{A_\star - A_i} \right)^{\beta}, \tag{5a}$$

$$A_\star = \frac{1}{1 - \left(L_{min} L_{max}^{-1} \right)^{1/\beta}} \tag{5b}$$

where A_i is the ice concentration and L_{min} and L_{max} are limits of floe length (here 8 and 300 m); $A_\star$ is introduced to avoid singularity. The change is applied to both air-ice and ice-water drag coefficients.

Another sensitivity experiment is conducted reducing the ridge sail height to keel depth ration $R_h = H_s / H_k$ from the default value 4 to 3. This parameter is used in the computation of pressure ridge statistics needed for the ridge form drag coefficient parameterization (Appendix A, equation (A4)). Its reduction by 25% increases dominance of ridge sails and means a greater influence by the air-ice drag and thus the atmospheric forcing.

We also tested for the impact of ice strength by simply doubling C_f, a model parameter that controls the compressive strength of the ice [*Flato and Hibler*, 1995], from 10 in FORM to 20 in another simulation referred to as FORM_Cf20. While a value of 10 is at the lower bound of the 9–17 range supported by the discrete particle ridge model study of *Hopkins* [1994], 20 is slightly above. The long-term annual mean ice strength increases from 22.3 kN/m in FORM to 39.9 kN/m in FORM_Cf20.

2.2. Ocean Surface Stress Calculation

Since we run CICE in a stand-alone configuration the model does not provide ocean surface stress (equation (1)) as a diagnostic but only the surface stress at the ice-water interface (equation (2b)), i.e., the surface stress for the ice-covered part of a model grid cell. We compute the surface wind stress on open water from daily mean model forcing fields of the wind speed using equation (2a) and a wind speed dependent drag coefficient according to equation (3). Then the ocean surface stress is derived following equation (1) for each model experiment using daily mean fields of sea ice concentration and ice-water stress from the respective simulation.

The drag coefficients over open water are therefore the same for all experiments discussed. However, their contribution to the total ocean surface stress depends on the open water fraction in each simulation. The open water drag coefficients in our experiments differ from those used in the PIOMAS simulation presented by *Martin et al.* [2014] because of the different wind forcing applied. Wind speeds in the NCEP-DOE-2
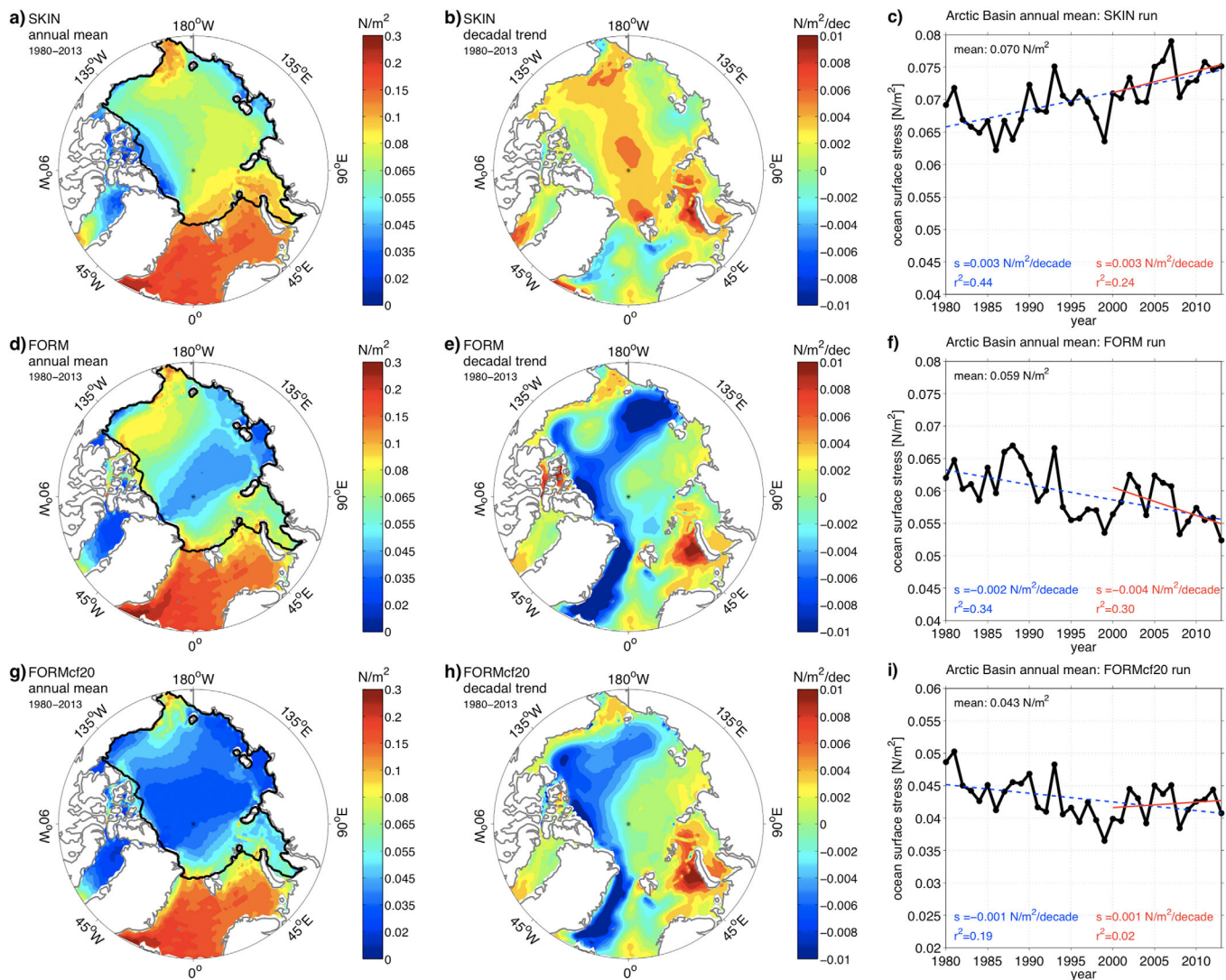
Figure 1. Maps of (a) annual mean total ocean surface stress averaged over the period 1980–2013 and (b) linear trends for the same period from SKIN. (c) Time series of annual mean ocean surface stress averaged over the Arctic Basin, which we define as the region enclosed by the bold black contour in panel (a), and linear trends for the periods 1979–2013 (dashed blue line) and 2000–2013 (red). Results of the (d–f) FORM experiment and (g-i) FORM_Cf20. Note, y axis limits in Figure 1i differ from Figures 1c and 1f though the range is the same.

reanalysis, which we use here, are about 1 m/s higher on average than those in the NCEP/NCAR reanalysis used by *Martin et al.* [2014]. *Lindsay et al.* [2014] compared daily mean wind speed of six reanalysis products with observations from North Pole drifting stations and found that wind speeds from NCEP-DOE-2, which are used here, are closer to observations from May to October (mean bias 0.3 m/s) while NCEP/NCAR wind speeds have the smaller absolute bias (−0.5 m/s) in the winter months November–April.

3. Results

The sea ice cover is an effective moderator of the momentum flux from the atmosphere into the ocean. Its key parameters ice concentration, thickness, and drift already affect the momentum transfer and we begin with briefly presenting results of experiment SKIN lacking the complexity of variable sea ice roughness. In this simulation the long-term mean ocean surface stress is largest in the Nordic and Barents seas (Figure 1a). Within the Arctic Basin, which is marked by a bold black outline, high surface stress is found in the Kara and Chukchi seas. In all these regions wind speeds are generally higher than over most parts of the Arctic Ocean. Least momentum is transferred into the Arctic Ocean where the sea ice is nearly immobile year-round, such as north of Greenland and the Canadian Archipelago as well as in the coastal areas of the Siberian shelf seas.
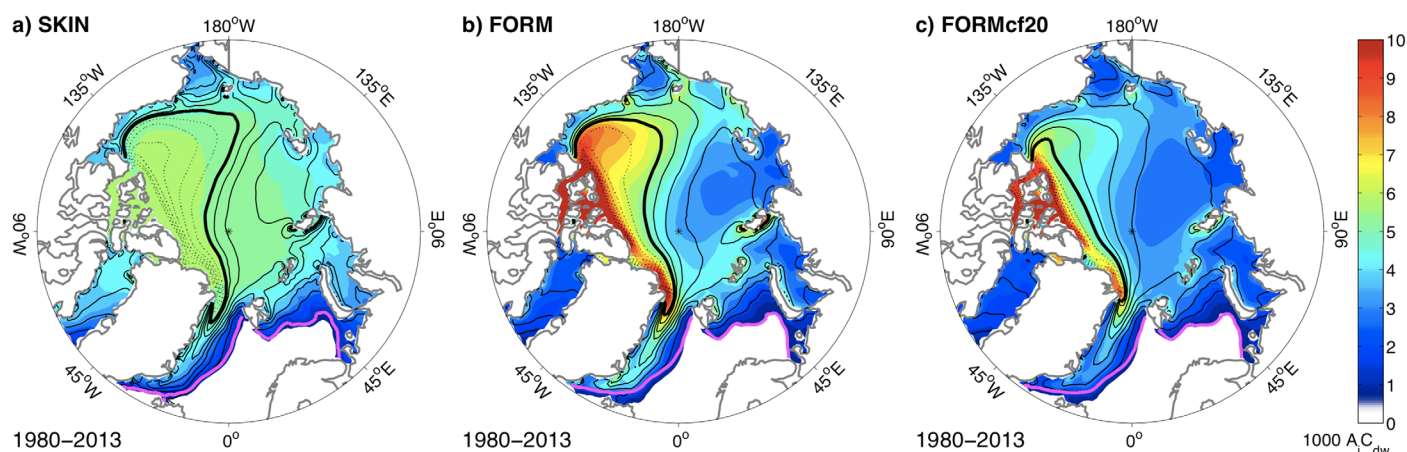
Figure 2. Annual mean ice-water drag coefficient multiplied by sea ice concentration (A_iC_{dw}) for (a) SKIN, (b) FORM, and (c) FORM_Cf20 averaged over the period 1980–2013. The sea ice edge (15% ice concentration) is marked by a magenta line. Black lines depict the mean ice thickness distribution in increments of 0.25 m up to 2 m (bold black line), followed by 0.5 m increments for ice thicknesses exceeding 2 m (dotted lines).

In the latter region the ice quickly melts after summer break up giving way to a less rough open water surface, which is most pronounced during the last decade of the simulation. In the central Arctic a belt of moderate ocean surface stress spans from the Alaskan to the European side of the Arctic Ocean.

The spatial distribution of the 1980–2013 ocean surface stress trend shows some regional inhomogeneity with strongest positive values north of Svalbard, in the central Arctic near the North Pole, and the Chukchi Sea and small negative values only occurring in the Laptev Sea and Bering Strait (Figure 1b). The Arctic Basin annual mean ocean surface stress is increasing at 0.0027 N/m^2 per decade during the study period 1980–2013 (Figure 1c). The predominantly positive trend in ocean surface stress in the SKIN run can be attributed to the overall thinning of the Arctic sea ice cover and the associated weakening, which reduces frictional losses within the ice cover so that more momentum is received by the ocean underneath.

Magnitude, spatial pattern, and trend of the annual mean ocean surface stress from the sea-ice only simulation SKIN are remarkably similar to those derived from the coupled sea ice-ocean model PIOMAS [*Martin et al.*, 2014] despite differences in atmospheric forcing (see section 2.2). No particular effort was made to produce this similarity. This demonstrates the suitability of the CICE model for answering qualitatively questions of momentum transfer into the Arctic Ocean related to sea ice characteristics.

In the following sections, we concentrate on the implications of introducing variable drag coefficients for the mean state and trends of ocean surface stress over the past three decades. The study area is limited to the Arctic Basin as defined in Figure 1a.

3.1. General Impact and Annual Mean
Introducing variable drag coefficients has little impact on the total Arctic sea ice area but reduces the total ice volume by about 5% and 15% in winter and summer, and Arctic-mean sea ice drift speed is slower during the summer months than in SKIN, which is discussed in more detail in *Tsamados et al.* [2014]. Most importantly, the added variability of the drag coefficients affects the spatial distribution and variability of the ice thickness and drift velocity with implications for the momentum flux into the ocean. The annual mean ocean surface stress of the FORM simulation is depicted in Figure 1d. Major differences to SKIN are found in the central Arctic, where the surface stress is lower by 30–50%, and in the Beaufort Sea, where ocean surface stress is about 30% higher than in SKIN. The strong gradient in ocean surface stress between the Beaufort Sea and the central and eastern Arctic in FORM originates from the distribution of the ice-water drag coefficient. In contrast to the SKIN simulation the sea ice surface roughness in FORM is much larger in the Beaufort Sea than in the region extending from the Laptev Sea to the central Arctic (Figures 2a and 2b). We find enhanced surface roughness expressed by an ice-water drag coefficient exceeding 6.5×10^{-3} (yellow and red colors in Figure 2b) in areas featuring an annual mean sea ice thickness of at least 2 m (bold black outline) and a significant amount of deformed sea ice. More than 25% of the ice area consists of deformed sea ice where the drag coefficient exceeds 6.5×10^{-3}. The Beaufort Sea is influenced by a tail of thick multiyear ice extending from the region

Table 1. Comparison of the Spatial Distributions of Ocean Surface Stress Magnitudes and Trends[a], and Linear Trends of the Annual Mean Ocean Surface Stress for Three Periods[b]

	Pattern Correlation of Mean			Pattern Correlation of Trend			Basin-Mean Trends (N/m^2 per decade)		
	Regression Coefficient	Correlation Coefficient	RMSE (N/m^2)	Regression Coefficient	Correlation Coefficient	RMSE (N/m^2)	1980–2013	1980–1999	2000–2013
SKIN	0.54	0.52	19.6×10^{-3}	0.17	0.35	61.9×10^{-5}	**0.0027**	0.0010	**0.0033**
FORM	*1.0*	*1.0*	*0.0*	*1.0*	*1.0*	*0.0*	*−0.0023*	*−0.0038*	*−0.0043*
FORM_beta03	1.02	1.0	0.5×10^{-3}	1.01	1.0	0.9×10^{-5}	−0.0024	−0.0038	−0.0044
FORM_beta14	0.95	1.0	1.8×10^{-3}	0.92	0.99	6.9×10^{-5}	−0.0019	−0.0036	−0.0038
FORM_Rh3	1.35	0.96	18.6×10^{-3}	1.56	0.98	38.6×10^{-5}	−0.0054	−0.0085	−0.0100
FORM_Cf20	0.72	0.85	19.2×10^{-3}	0.81	0.84	22.6×10^{-5}	−0.0013	−0.0041	0.0008

[a]Compared are spatial distribution of long-term (1980–2013) annual mean ocean surface stress magnitudes and trends from FORM to those of all experiments by means of pattern correlation, for which regression and correlation coefficients are given, and root mean squared error (RMSE).

[b]Trends of the annual mean ocean surface stress for three periods are listed in the third column with those in bold that are significant at *p<0.02 according to a two-tailed t-test using absolute sample size N=34*. Default settings used in FORM are $\beta=0.5$, $R_h=4$, and $C_f=10$. Only the region of the Arctic Basin (black line in Figure 1a) was considered for these statistics. The respective patterns and time series of SKIN, FORM, and FORM_Cf20 are displayed in Figure 1.

north of Canada, where sea ice mass is converged by the mean ice drift circulation. In contrast, the relatively thin and young first-year ice cover of the central Arctic has annual mean ice-water drag coefficients of less than 4.0×10^{-3} (blue colors).

The impact of changing the floe size distribution is relatively small and annual mean results of the experiments FORM_beta03 and FORM_beta14 are very similar to those of FORM (Table 1). We see that $\beta=0.3$ yields slightly larger mean and trends (regression coefficient >1) and $\beta=1.4$ smaller ocean surface stress (regression coeff. <1) than the default of $\beta=0.5$ in FORM. Altering the ridge sail height to keel depth ratio R_h toward a greater dominance of the sails in FORM_Rh3 increases the magnitude of the ocean surface stress and its interannual variability by 27% and 40%, respectively; for comparison, changing β yields deviations smaller than 10%. However, similar to β changing R_h does not impact the spatial distributions of ocean surface stress magnitude and trends significantly (correlation coefficients >0.95, Table 1). And emphasizing the impact of sails simply increases the negative ocean surface stress trend for all periods (Table 1). These results underline the robustness of the differences between FORM and SKIN runs with respect to parameter choices in the form drag parameterizations itself, and we can focus the discussion of the sensitivity experiments on the run with enhanced ice strength, FORM_Cf20.

In the sensitivity run FORM_Cf20 the internal ice force is enhanced by 0.004 N/m^2 (24%) and the sea ice drifts slower at only 0.058 m/s instead of 0.072 m/s in FORM in the annual Arctic Basin mean. Most prominently, experiment FORM_Cf20 has much thinner ice in the Beaufort Sea than FORM lacking the tail of thick multiyear ice reaching into the Beaufort Gyre (black contours in Figure 2c). Consequently, annual mean ice-water drag coefficients larger than 6.5×10^{-3} are only found in a narrow band north of Greenland and the Canadian Archipelago. In most parts of the Arctic Ocean the annual mean ice-water drag coefficient is even lower than in the SKIN run. The stronger ice is being less deformed and hence has a smoother surface. Overall, the annual mean ocean surface stress magnitude in FORM_Cf20 is smaller than in the SKIN and FORM simulations and the region of low surface stress spreads out farther toward Alaska than in FORM (Figure 1g).

In FORM, the local trends of ocean surface stress for 1980–2013 are spatially more variable than in SKIN (Figure 1e). Most prominent is the decline in ocean surface stress in the Siberian Sea, central Arctic and along the coast of Greenland and the Canadian Archipelago. Positive trends are found in the Barents and Kara seas and in the Chukchi Sea similar to the SKIN results. Also, the core of the Beaufort Gyre stands out for its positive trend. In FORM_Cf20 this latter feature is absent and the negative trend in the East Siberian Sea is less pronounced.

In FORM, areas with declining ocean surface stress dominate the basin-wide mean and we find that the Arctic Basin annual mean ocean surface stress decreases at −0.0023 N/m^2 per decade from 1980 to 2013 with a slightly steeper decline of −0.0043 N/m^2 since 2000 (Figure 1f), which is in stark contrast to the increase suggested by the SKIN simulation with constant sea ice surface roughness. For both FORM and SKIN the 34 year trend is significant at $p<0.01$ according to a two-tailed t-test based on absolute sample size. Increasing the sea ice strength in FORM_Cf20 damps the overall decline in ocean surface stress to −0.0013 N/m^2 per decade. Computing trends separately for the periods 1980–1999 and 2000–2013, shows that the decline is in fact as strong as in FORM for the first period (−0.0041 N/m^2 per decade, Table 1) but turns into an increase after 2000. This
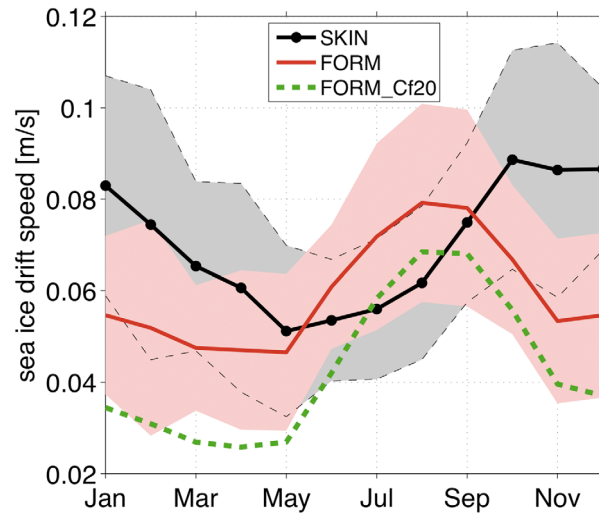
Figure 3. Annual cycle of Arctic Basin monthly mean ocean surface stress averaged over the period 1980–2013; shading shows ± 2 standard deviations indicating interannual variability over this period.

increase is depicted by a red line in Figure 1i (0.0008 N/m² per decade) and resembles the positive trend in SKIN.

Another major difference between SKIN and all simulations with variable drag coefficients is the seasonal timing of the peak in ocean surface stress. Figure 3 shows annual cycles of ocean surface stress and we note that with variable drag coefficients the maximum ocean surface stress is found in August instead of October. Moreover, ocean surface stress in fall and winter (October–April) is significantly lower than in SKIN but exceeds the SKIN value during the summer months. The seasonal cycles of ocean surface stress and variable drag coefficients is discussed in more detail in *Martin et al.* [2014] and *Tsamados et al.* [2014].

Why are the long-term trends from SKIN, FORM and FORM_Cf20 so different? Why does ocean surface stress peak in summer in simulations with variable drag coefficients? In order to answer these question we need to take a more detailed look at the various drivers of ocean surface stress variability under both winter and summer conditions separately.

3.2. Ice Strength and Ridge Form Drag in Winter

In order to understand what drives long-term changes in ocean surface stress in the Arctic each variable term of the ocean surface stress relationship (equations (1) and (2)) is looked at in the following. The Arctic region experiences a strong annual cycle and sea ice conditions differ greatly between the winter season, which here is represented by a January–March mean, and summer (July–September mean). Hence, we study the decomposition of the ocean surface stress for both seasons separately beginning with winter.
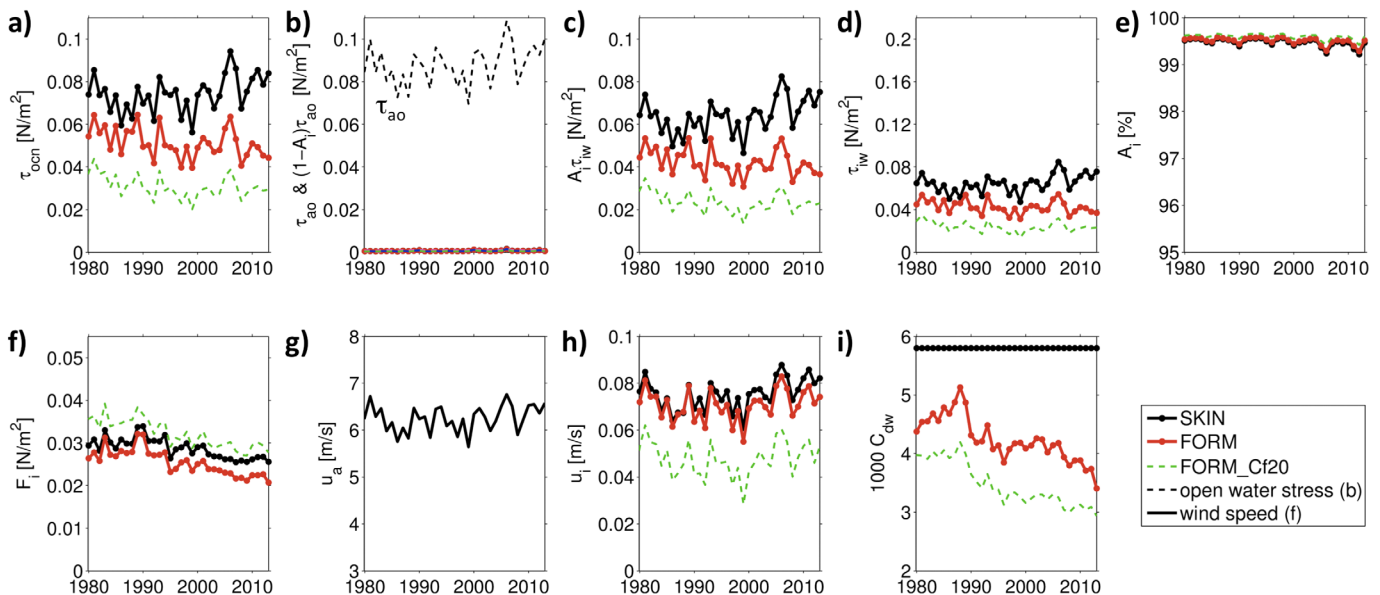

Figure 4. (a) Time series of the total ocean surface stress for the winter season (January–March mean). Decomposition into individual terms of equations (1) and (2): (b) wind stress on open water (potential magnitude τ_{ow}, dashed black line, and weighted by open water area fraction $(1-A_i)\tau_{ow}$, all other lines), ice-water surface stress weighted by (c) ice concentration and (d) actual magnitude, (e) sea ice concentration, (f) sea ice interaction force, (g) wind speed at 10 m height (from model forcing), (h) sea ice drift speed, and (i) total ice-water drag coefficient. Values represent Arctic Basin-wide averages (see outline in Figure 1a). Note the difference in y axis scale between Figure 4c and Figure 4d.
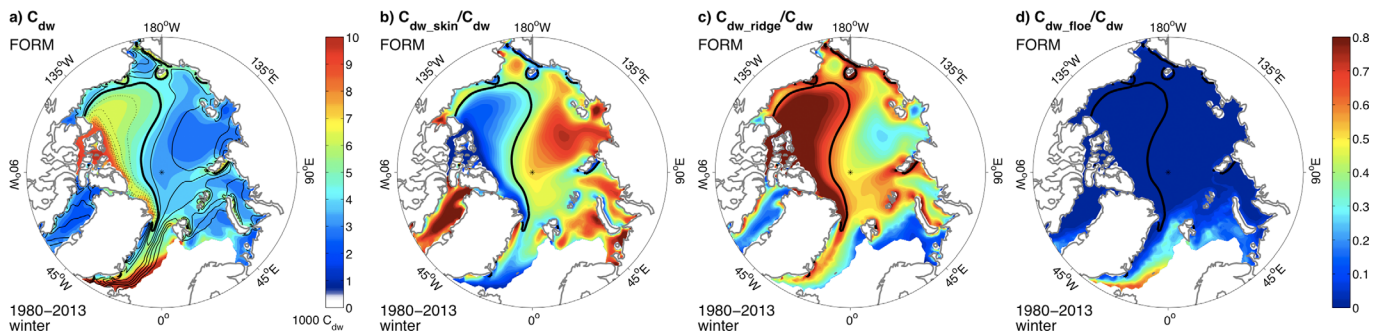
Figure 5. Winter (January–March) (a) mean ice-water drag coefficient C_{dw} and (b) fractions of skin drag C_{dw_skin}, (c) ridge form drag C_{dw_ridge}, and (d) floe edge form drag coefficients C_{dw_floe} of the total ice-water drag coefficient C_{dw} averaged for the period 1980–2013 from simulation FORM. Thin black lines depict the mean ice thickness distribution in increments of 0.25 m between 0.5 and 2 m (bold black line), thin dotted lines ice thicknesses exceeding 2 m in 0.5 m increments. Only values within the sea ice edge (15% ice concentration) are shown.

Figure 4a shows time series of Arctic Basin winter mean ocean surface stress. Similar to the annual mean trends discussed above, we find an increase of 0.0030 N/m^2 per decade for SKIN (black), an overall decrease of −0.0028 N/m^2 per decade for FORM (red), and a negative but weaker trend of −0.0021 N/m^2 per decade for FORM_Cf20 (dashed green). All of these winter trends for the period 1980–2013 are significant at $p<0.03$. We compute the basin-mean wind stress on open water from the model forcing (equation (2a)) to show the magnitude and evolution of the surface stress in the absence of sea ice for comparison. In winter this potential wind stress on open water (Figure 4b, dashed black line) is larger than the actual ocean surface stress, which is an indication of the ice cover limiting momentum transfer into the ocean in this season. The potential of sea ice to damp momentum transfer is discussed in more detail in section 3.5. Despite its higher magnitude, open water stress contributes only a tiny fraction to the total surface stress and most of the momentum flux has to pass through the ice because of the high ice concentration of more than 99% in winter (Figures 4b–4e). The high compactness of the winter sea ice cover also causes significant internal stress, which results in an ice interaction force countering the wind forcing [e.g., *Steele et al.*, 1997, Figure 11]. This ice interaction force, defined as the divergence of the ice internal stress tensor, is decreasing after the late 1980s (Figure 4f) coinciding with a reduction in mean ice thickness of more than 1 m in all simulations (not shown). In the absence of a significant trend in the wind forcing (Figure 4g), increases in sea ice drift speed (Figure 4h) and ocean surface stress (Figure 4a) in SKIN can be related to the reduction of the ice interaction force. As Figure 4f shows the decline of the ice interaction force is very similar for all simulations. Then why did ocean surface stress decline in the simulations with variable drag coefficients?

The spatial distribution of the variable ice-water drag coefficient follows closely the mean ice thickness distribution in winter (Figure 5a). Decomposed into its three contributors (equation (4)) we find that the under ice roughness in winter is dominated by the skin drag and ridge form drag coefficients (Figures 5b and 5c). The fractions where calculated from daily mean model output before being averaged for the whole period 1980–2013. Form drag by ridges is dominant where the mean ice thickness exceeds 2 m (bold black line) and skin drag is larger where the ice is thinner (and less deformed), which is in particular the case in the Laptev Sea and north of it. This direct balance between skin drag and ridge form drag coefficients is inherent to the parameterization, which accounts for the sheltering effect reducing the skin drag in the presence of ridges. With a highly compact sea ice cover (mean $A_i>99\%$) and simulated floe diameters of 100–300 m, form drag by floe edges is practically absent in the Arctic Ocean in winter and only plays a role in the marginal ice zone (MIZ), which is found further south in this season, for instance in the Nordic Seas (Figure 5d).

Since the late 1980s the sea ice volume in the Arctic Basin has been declining mostly at the expense of deformed sea ice (Figure 6a). This is associated with a drop in Arctic basin winter mean ice thickness from 2.5 m in 1988 to 1.4 m in 2013 in FORM. Consequently, the form drag caused by ridges has been declining, too, and with it the total ice-water drag coefficient (Figure 6b). The skin drag and floe edge drag coefficients remained mostly stable. A slight increase of the skin drag coefficient (blue line) can be related to a reduced sheltering effect from fewer and smaller ridges according to the skin drag parameterization (see equation (A7)). We also find that the basin-mean ridge form drag coefficient was nearly four times the skin drag coefficient at its peak in 1988 but has declined to almost the same magnitude as the skin drag coefficient in
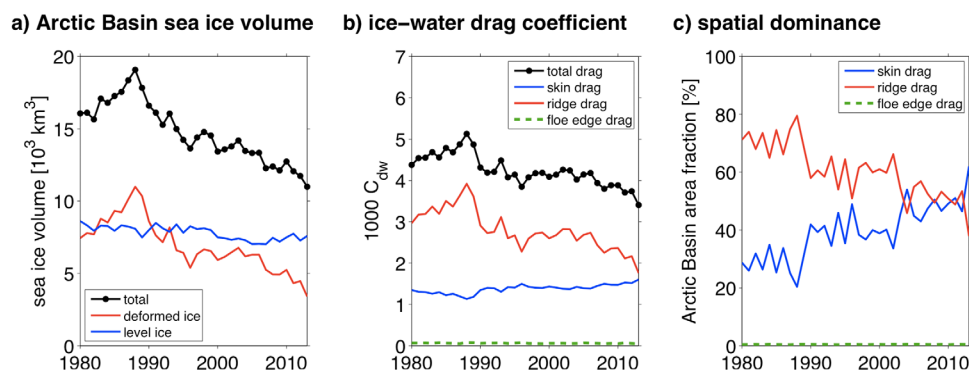
Figure 6. (a) Winter mean total sea ice volume in the Arctic Basin (see outline in Figure 1a) (black line) and volume of deformed (ridged) ice in red and undeformed (level) ice in blue. (b) Winter mean total ice-water drag coefficient (C_{dw}, black), skin drag (C_{dw_skin}, blue), ridge form drag (C_{dw_ridge}, red), and floe edge form drag coefficients (C_{dw_floe}, dashed green) averaged over the Arctic Basin. (c) Fraction of the Arctic Basin area in which the respective drag coefficient contributes most to the total ice-water drag coefficient. All results are from experiment FORM.

recent winters. The retreat of thick, heavily ridged ice also led to a growing spatial dominance of skin drag (Figure 6c). We diagnose the spatial dominance of a particular drag coefficient for a given year by computing the total area of all grid cells in which this drag coefficient is larger than the other skin or form drag coefficients, i.e., in which it contributed most to the total ice-water drag coefficient. This area is then divided by the total Arctic Basin area covered by sea ice (grid cells with $A_i < 5\%$ are excluded). While the calculation is done with daily mean model output, the numbers displayed in Figure 6c are seasonal January–March averages. The time series show that in the 1980s the ridge form drag coefficient dominated the total ice-water drag coefficient in more than 70% of the Arctic Basin area while this is the case in less than half the area after 2003.

For the winter season, we conclude that the loss of thick deformed sea ice in the Arctic Ocean has led to a significant decline of the form drag coefficient, an increased spatial dominance of the generally lower skin drag, and thus a reduction in the total ice-water drag coefficient. Simply spoken, the sea ice surface has become smoother over the past three decades. In our simulation FORM, this loss of ice roughness (Figure 4i) has a greater impact on the ocean surface stress than the simultaneous decline of the ice interaction force (Figure 4f) yielding an overall reduction of the ocean surface stress in winter (Figure 4a). This effect is absent in SKIN, which only uses a constant ice-water drag coefficient. In the simulation with stronger sea ice (FORM_Cf20), the ice interaction force follows a similar trend but is capable of counteracting the downward trend of the total ice-water drag coefficient, because the latter is smaller and the ice interaction force is larger than in FORM (Figures 4i and 4f). Thus, the overall decline of the ocean surface stress is smaller in FORM_Cf20 than in FORM and a transition toward a positive trend—as in SKIN—can be seen for the last 13 years.

3.3. Ice Concentration and Floe Edge Form Drag in Summer

For the summer season (July–September), we find that the basin-mean ocean surface stress in SKIN is smaller than in simulations with variable drag coefficients, except for FORM_Cf20 (Figure 7a). This is contrary to winter when SKIN features the highest ocean surface stress among our experiments (cf. Figure 4a). Here we include the two sensitivity experiments with altered floe size parameter β because in summer they notably differ from FORM. The summer mean ocean surface stress decreases over the period 1980–2013 at a rate of -0.0035 N/m^2 per decade in all runs with variable form drag coefficients except in FORM_Cf20, in which the decline is only -0.0023 N/m^2 per decade (dashed green line in Figure 7a). All these trends are significant at $p < 0.05$ according to a two-tailed t-test. There is no significant trend in SKIN (black line).

In summer other processes than in winter control the momentum transfer into the Arctic Ocean and the presence of sea ice leads to an increase of the ocean surface stress. The open water wind stress multiplied by the actual open water area (Figure 7b) has been steadily increasing while the ice-water stress multiplied by sea ice concentration (Figure 7c) has been declining since the end of the 1980s, which is due to the rapid retreat of the Arctic sea ice cover in summer from an average sea ice concentration of about 60% in the 1980s to less than 30% in 2012 in all simulations (Figure 7e). Note that the basin-mean wind forcing itself has no trend (Figure 7g). Sea ice concentration plays a major role in determining summer ocean surface
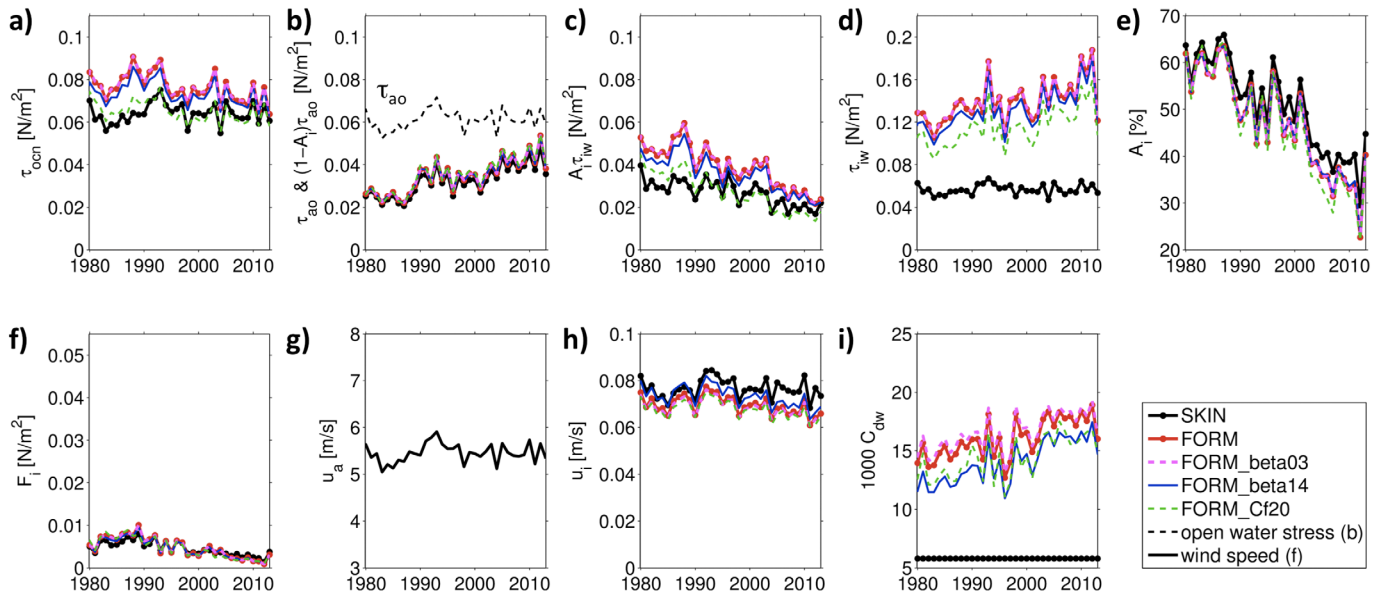
Figure 7. Same as Figure 4 but for the summer season (July–September mean).

stress whereas the ice interaction force is reduced to a marginal contribution (Figure 7f), in contrast to winter conditions discussed above. Also opposite to winter, the ice-water drag coefficient in the experiments with form drag is larger than the constant drag coefficient in SKIN; variable drag coefficients have a four times larger magnitude in summer (Figure 7i). This explains why ocean surface stress in FORM is higher than in SKIN during summer but lower during winter and leads to the shift in the annual cycle of ocean surface stress shown in Figure 3. Further, the variable ice-water drag coefficients are increasing in summer over the period 1980–2013 whereas they are decreasing in winter (cf. Figure 4i). Why is that and what is the consequence?

The basin-mean time series show that the increasing surface roughness is reflected in the ice-water surface stress (Figure 7d) but the effect is outbalanced by the strong negative trend in sea ice concentration (Figure 7e) and the product is an overall decrease (Figure 7c). Figure 8 shows maps of the total ice-water drag coefficient and the fractional contributions by skin drag, ridge and floe edge form drag for the summer season. The distribution of the total ice-water drag coefficient is different from the one in winter (cf. Figure 5a). The MIZ is now located within the Arctic Basin and the total ice-water drag coefficient can be as large as 30×10^{-3} where the sea ice concentration is below 40%. In FORM these areas are characterized by floe sizes of less than 50 m in diameter, often just around 10 m (not shown). Although the ice-water skin drag coefficient has a similar magnitude as in winter, between 1×10^{-3} and 2×10^{-3}, it plays only a marginal role in summer even within the pack ice (Figure 8b) because its magnitude is exceeded by the ridge and floe edge form drag coefficients. Form drag in areas exceeding 80% sea ice concentration, which is associated with a mean ice thickness of at least
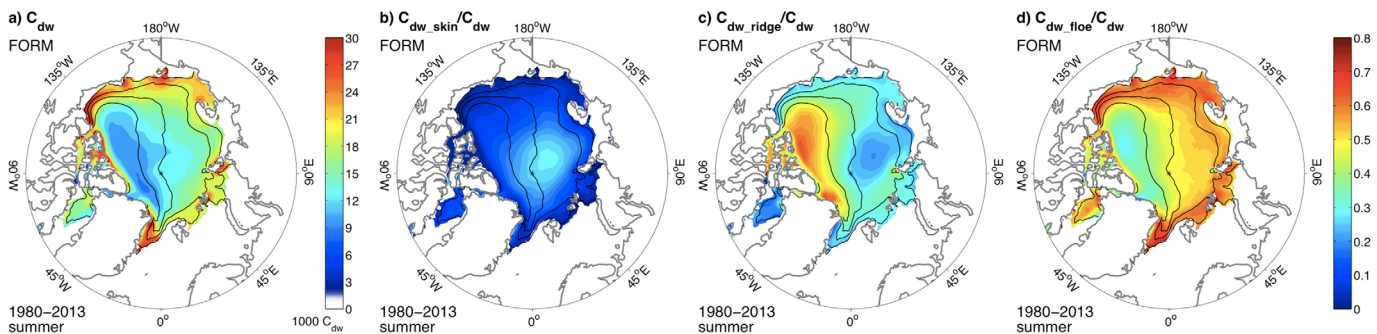
Figure 8. Summer (July–September) (a) mean ice-water drag coefficient C_{dw} and (b) fractions of skin drag C_{dw_skin}, (c) ridge form drag C_{dw_ridge}, and (d) floe edge form drag coefficients C_{dw_floe} of the total ice-water drag coefficient C_{dw} averaged for the period 1980–2013 from simulation FORM. Thin black contours indicate sea ice concentration from the same period between 20% and 80% in 20% intervals. Only values within the sea ice edge (15% ice concentration) are shown.

Figure 9. (a) Summer mean total sea ice area in the Arctic Basin (see outline in Figure 1a) (black) and area of deformed (ridged) ice in red and undeformed (level) ice in bl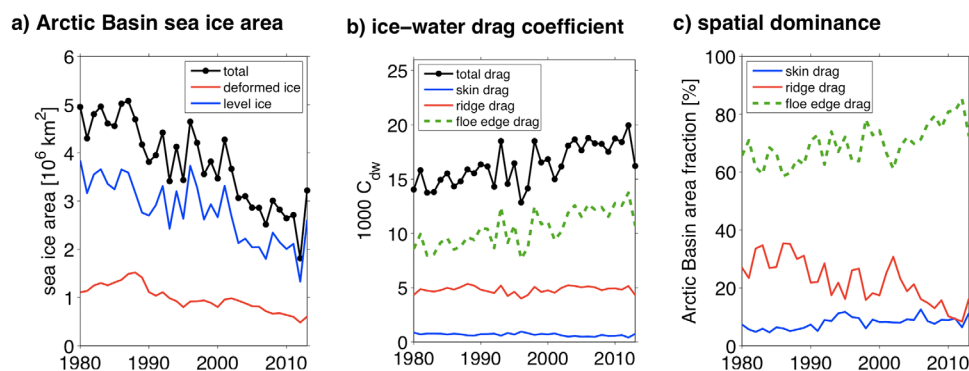ue. (b) Summer mean total ice-water drag coefficient (C_{dw}, black), skin drag (C_{dw_skin}, blue), ridge form drag (C_{dw_ridge}, red), and floe edge form drag coefficients (C_{dw_floe}, dashed green) averaged over the Arctic Basin. (c) Area fraction of the Arctic Basin in which the respective drag coefficient contributes most to the total ice-water drag coefficient. All results are from experiment FORM.

2 m, mostly originates from ridges (Figure 8c). The respective ice-water drag coefficients range between 6×10^{-3} and 9×10^{-3} in summer similar to those in winter. Such values are small compared to the ice-water floe edge form drag coefficient, which can reach values of 20×10^{-3} to 30×10^{-3} in this season. In regions of thin ice and in particular where the ice concentration is lower than about 60%, form drag by floe edges thus dominates the total ice-water drag coefficient (Figure 8d). Note, the impact of the high ice-water drag coefficient in the MIZ on the model ocean is diminished by the ice concentration weighted averaging of the surface stress over the entire grid cell (equation (1)). Similarly, measurements in the MIZ will capture a roughness length scale that represents a mixture over ice and open water resulting in total ocean surface drag coefficients presumably smaller than 20×10^{-3}. However, recent observations support a median ice-water drag coefficient of 10×10^{-3} [*Cole et al.*, 2014].

The retreat of the sea ice cover is a major driver of changes in ocean surface stress. Figure 9a shows that the Arctic Basin lost about half of its sea ice cover between the late 1980s and recent summers. This reduction occurred at the expense of both deformed and level ice though the trend is steeper for the latter. While this evolution leaves basin-mean values of skin and ridge form drag coefficients mostly unchanged over this period the basin-mean floe edge form drag coefficient has increased by 50% (Figure 9b) because of a growing area being covered by less compact ice and small floes typical of the MIZ. Consequently, the total ice-water drag coefficient is now dominated by floe edge form drag in a larger area of the Arctic basin (green dashed line in Figure 9c). This includes parts of the Beaufort Sea, the entire Chukchi Sea and a wide region between the North Pole and the Siberian shelf break, in which the total ice-water drag coefficient has increased from 10×10^{-3} before 2000 to 18×10^{-3} in recent years (not shown). The ridge form drag coefficient loses spatial influence due to the simultaneous thinning of the ice cover (red line). Thick pack ice in which the ridge form drag coefficient dominates in summer is only found in a rapidly shrinking area north of Greenland and the Canadian Archipelago.

In summary, the ice-water drag coefficient has increased in summer and with it the ice-water stress magnitude, the open water surface stress has not changed, and the total ocean surface stress has a negative trend in simulations FORM, FORM_beta03, and FORM_beta14. The only trend that explains this behavior is the overall reduction in sea ice area, which gives way to vast regions of open water with a much smaller surface roughness and thus forces total ocean surface stress to decline. We conclude that enhanced form drag exerted by floe edges in a widened MIZ does not outbalance the negative impact of complete sea ice retreat on the basin-mean ocean surface stress. Locally, MIZ conditions yield higher surface stress but only for short periods of time since conditions within the MIZ and the location of the MIZ can change daily depending on the wind. For basin-mean ocean surface stress holds in both cases, with and without variable drag coefficients: the farther the sea ice retreats, the less momentum the Arctic Ocean will receive during summers.

3.4. Optimal Ice Concentration and Thickness

Sea ice concentration and thickness data have been utilized in the past in computations of the surface roughness and neutral drag coefficients of the Arctic Ocean. For example, *Andreas et al.* [2010] proposed a
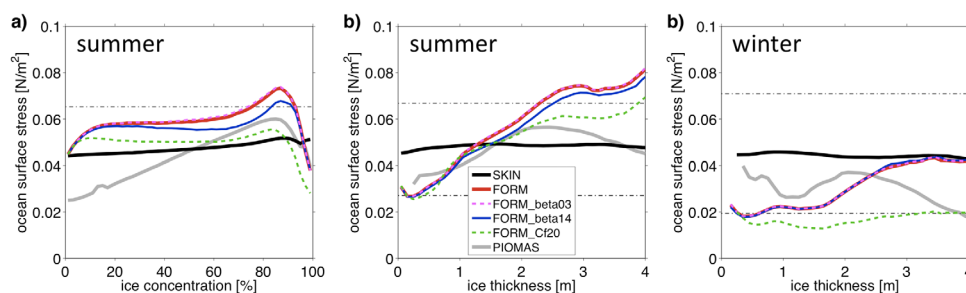
Figure 10. Ocean surface stress as a function of sea ice (a) concentration and (b, c) thickness. Sea ice concentration (thickness) from daily mean model output including all ocean grid cells within the Arctic Basin (Figure 1a) was sorted into bins with 2% (0.1 m) increments. The depicted lines connect the medians computed from the distribution in each bin. Thin dash-dotted lines indicate the median in the 0–2% (0–0.1 m) bin of experiment SKIN plus/minus twice the standard deviation of the distribution in this bin indicating significant deviations from the open water case. The distributions include all days of each summer/winter season (July–September/January–March) from the period 1980–2013. PIOMAS output from *Martin et al.* [2014] was treated in the same way to be included for comparison (gray lines). Note, here ice thickness is sea ice volume per ice-covered grid cell area, i.e., actual thickness. The legend in Figure 10b holds for all plots.

parameterization of the air drag coefficient based exclusively on ice concentration while *Tremblay and Mysak* [1997] assumed a linear relation between the drag coefficient and ice thickness in their model. Here we present the relationship between the ocean surface stress to ice concentration and thickness in our computations stripped of their dependencies on space and time. For this purpose we group daily mean model output of ice concentration and thickness into bins of 2% and 0.1 m width including all grid cells within the Arctic Basin (see black outline in Figure 1a) and from all years of the period 1980–2013. For ice concentration we limit this computation to the summer season of months July–September, because sample sizes for bins below ∼80% ice concentration are extremely low otherwise. For ice thickness we look at summer and winter (January–March) separately. Here sea ice thickness is the actual thickness of floes, i.e., ice volume per ice-covered area, and is calculated from daily mean model output of mean ice thickness (ice volume per grid cell area) and ice concentration considering only data with a minimum concentration of 5%. The binning enables us to calculate the mean ocean surface stress associated with the ice concentration (or thickness) of each bin. We normalize the daily mean ocean surface stress by dividing by the square of the daily mean wind speed and multiplying with the square of the long-term basin mean value of 5.5 m/s. This accounts for variations in wind forcing, which are related to, for instance, the large-scale circulation and the stability of the atmospheric boundary layer and may bias the dependencies of ocean surface stress to be demonstrated. Lines in Figure 10 connect the bin median values of these normalized surface stresses, thus representing the general dependency of the ocean surface tress on sea ice concentration and thickness.

In all simulations ocean surface stress peaks at an ice concentration of about 80–90% and is smallest for the extremes of 0% (open water) and 100% ice concentration (Figure 10a). The ocean surface stress in the 0–2% bin is set by the wind stress on open water. In all experiments open water surface roughness is derived from equation (3) and is on average less than the sea ice surface roughness though the difference is small in SKIN. Therefore ocean surface stress increases with increasing sea ice concentration up to an ice concentration of 80–90%, which thus can be viewed as optimal for momentum transfer into the ocean. At even higher concentrations ocean surface stress decreases due to the ice interaction force countering the wind forcing. The ice interaction force grows exponentially from a negligibly small value below 70% to a mean value of 0.04 N/m² at 100% ice concentration (not shown). Additionally, floe edges do not provide drag in such compact ice conditions and densely aligned ridges are associated with strong sheltering limiting their potential to provide drag. The dash-dotted line in Figure 10a marks the median plus twice the standard deviation of the distribution in the 0–2% ice concentration bin, i.e., the 95th percentile of the ocean surface stress distribution over open water. This shows that the median ocean surface stress at the optimal ice concentration of 80–90% is significantly enhanced compared to stress on open water in runs FORM, FORM_beta03, and FORM_beta14. The mean ocean surface stress (not shown) includes exceptionally high stress values and thus is significantly enhanced at a wider range of ice concentrations (65–95%) than the median. The peak at the optimal ice concentration is not significant in SKIN and FORM_Cf20, however.

The peak of optimal ice concentration is also shaped by the variable drag coefficients (Figure 11a). The difference between FORM, FORM_beta03, and FORM_beta14 is best illustrated by Figure 11b: the peak of the
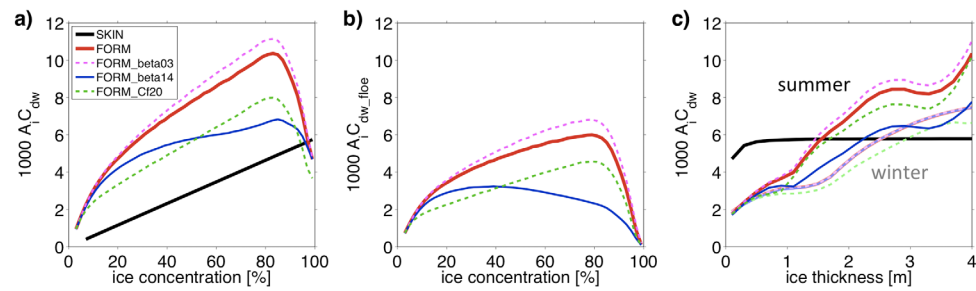
Figure 11. (a) Total ice-water drag coefficient weighted by sea ice concentration ($A_i C_{dw}$) as a function of sea ice concentration from summer months July–September of 1980–2013. The drag coefficients are multiplied by ice concentration to indicate their decreasing effect on total ocean surface stress with increasing open water area fraction. (b) Same as Figure 11a but for the ice-water floe edge form drag coefficient (C_{dw_floe}). (c) Total ice-water drag coefficient as a function of actual sea ice thickness, i.e., sea ice volume per ice-covered grid cell area, for summer (July–September, upper curves) and winter (January–March, lower pale-colored curves) of the period 1980 to 2013. All curves represent bin means and are based on daily mean model output (see caption of Figure 10 for details). The legend in Figure 11a holds for all panels.

floe edge form drag coefficient is at 80–85% for a β value of 0.3 to 0.5 (dashed magenta and red curves) whereas $\beta = 1.4$ (blue curve) shifts the peak to lower ice concentrations of 30–40% and reduces the magnitude by about a factor of 2. Increasing the sea ice strength significantly also reduces the magnitude of the floe edge form drag coefficient but does not affect the position of its peak (green dashed curve).

In contrast to ice concentration, ocean surface stress increases steadily with increasing sea ice thickness though not in experiment SKIN, in which the surface stress is not a function of ice thickness and almost constant at 0.05 N/m² (Figure 10b). In FORM ocean surface stress is significantly lower at 0.1 m thickness (~0.03 N/m²) and higher at 4 m (0.08 N/m²) intersecting the curve of SKIN at about 1.2 m ice thickness. This increase in ocean surface stress becomes significant at $p < 0.05$ with respect to the open water surface stress in FORM above a thickness of about 1.5 m. In winter, ocean surface stress in SKIN maintains about the same level as in summer (0.04 N/m²). In the runs with variable drag, surface stress is less for ice thinner than 3 m and similar for thicker ice (Figure 10c). Only FORM_Cf20 produces a constantly lower surface stress of less than 0.02 N/m² at all ice thicknesses. We conclude that the thicker the ice the more drag it provides. Further, an optimal ice thickness may exist at 2–3 m thickness, above which the growing ice interaction force potentially (out)balances the gain in drag. The associated peak in ocean surface stress is less pronounced than the one at the optimal ice concentration however.

The increase of ocean surface stress with ice thickness is tied to increasing surface roughness in the simulations with variable drag coefficients (Figure 11c). In our simulations the ridge form drag coefficient is a function of ridge height and spacing (equation (A4)), which depend on the ice concentration and deformed ice volume. The latter is closely related to the ice strength and ridging rate as parameterized in CICE [*Flato and Hibler*, 1995; *Lipscomb et al.*, 2007]. In addition, the floe edge form drag coefficient increases with ice thickness because it is a function of the freeboard and draft of the ice floes (equation (A5)). The contribution of the floe edge form drag to the total ice-water drag is only marginal in high ice concentration conditions and therefore we only observe a separation of the lines depicting the ice-water drag coefficient for FORM, FORM_beta03 and FORM_beta14 in Figure 11c for the summer but not for the winter season (pale colors). Due to the lack of floe edge form drag the latter season is characterized by smaller total ice-water drag coefficient.

3.5. Amplification of Momentum Transfer

The results presented in the previous sections indicate that on average sea ice has a rougher surface than open water. This enables a larger momentum flux into the ocean through sea ice in free drift, i.e., the ice drift responds directly to the wind forcing because ice interaction forces are negligibly small, than would be transferred under ice-free conditions. As shown above, most amplification occurs at an optimal ice concentration of about 80–90%. But does sea ice always amplify momentum transfer or are there situations in which it damps the exchange flux and ocean surface stress is reduced in the presence of ice?

We define an *amplification index* as the ratio of ocean surface stress (equation (1)) divided by the (potential) wind stress on open water (equation (2a)). This ratio equals unity if the surface stress on the ocean is the
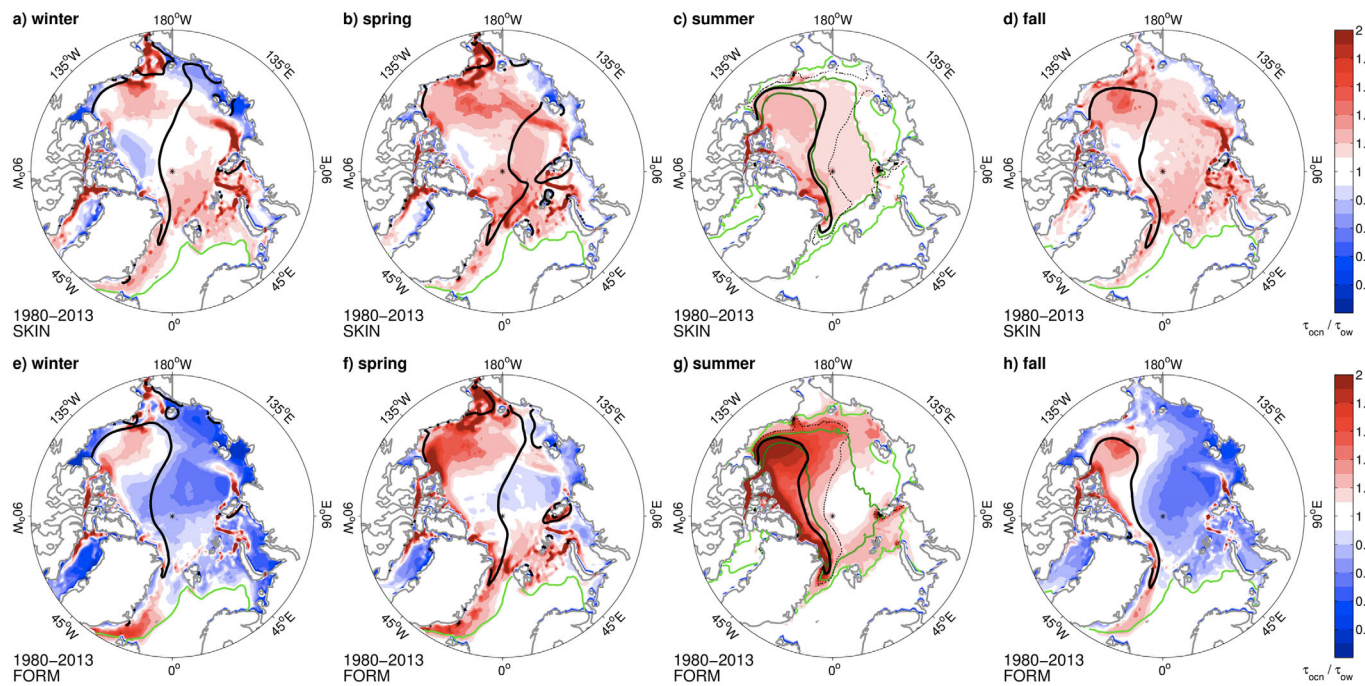
Figure 12. Ratio of total ocean surface stress to open water surface stress (τ_{ocn}/τ_{ow}) demonstrating the potential of sea ice to reduce or increase momentum transfer into the ocean. Open water surface stress only depends on wind speed (equation (2a)) from the model forcing and can thus be calculated also for ice-covered areas. Total ocean surface stress is computed according to equation (1) using daily mean model output of ice-water stress from (a–d) SKIN and (e–h) FORM. The daily ratios are then averaged to present season averages for (a, e) winter (January–March), (b, f) spring (April–June), (c, g) summer (July–September), and (d, h) fall (October–December). Black contours depict ice thickness isolines of 1 m (thin dotted, summer only) and 2 m (bold solid); green contours depict isolines of ice concentration at 15% (bright green) and—in summer only—at 50% (green) and 80% (dark green, nearly aligned with the 2m thickness isoline).

same under the ice as in the absence of sea ice. The index is greater (smaller) than unity in case the ocean surface stress exceeds (lags) the potential wind stress; then sea ice amplifies (damps) the momentum transfer into the ocean.

Figure 12 shows maps of the amplification index for all four seasons from SKIN and FORM. For the control experiment SKIN, in which a constant ice-water drag coefficient is used, we find that sea ice helps to increase the momentum flux into the ocean in most areas of the Arctic and in all seasons. As in the case of the optimal sea ice concentration discussed above this effect relates to the contrast between sea ice and open water surface roughness, which is prescribed in SKIN. Accordingly, index values of 1.1 and more do not occur below ice concentrations of 50% (middle green line in Figure 12c) and values of more than 1.2 are only reached in areas with at least 80% ice concentration (dark green line). Only where the ice is nearly immobile, on the Siberian shelf from fall to spring and north of Canada in winter, does sea ice shield the ocean from momentum influx from the atmosphere (index $<$1).

In the experiments with freely evolving sea ice drag coefficients this is different. Figures 12e–12h show results from FORM indicating strong regional differences and a pronounced seasonal cycle of the amplification index. While sea ice impedes momentum transfer in winter (Figure 12e) it amplifies the ocean surfaces stress in summer (Figure 12g), meaning the surface stress under the ice is higher than it would be in the absence of sea ice. The damping effect can be as big as 60% (index of 0.4) and amplification can exceed 100% (index of 2.0). In summer sea ice is mostly in free drift and either has no effect (white area extending from the Laptev Sea to the North Pole) or enhances momentum transfer in areas where the ice is thicker and form drag by ridges and floe edges make a significant contribution (Figure 12g, black lines indicate the ice thickness distribution). Then, going into fall, open water areas refreeze forming smooth thin ice and this has a large damping effect on the ocean surface stress (Figure 12h). Only when this ice deforms and thickens over the winter season—observe the bold black line of 2 m mean ice thickness expanding from fall to spring—the damping effect is lessened, turning into amplification in spring (Figure 12f). Note, while sea ice concentration governs the spatial distribution of the amplification index in SKIN in summer, its impact in FORM is minor and ice thickness governs the index pattern instead.

In FORM the index is decreasing in most areas over time (not shown) because the ocean surface stress is decreasing in all seasons whereas the open water wind stress has no significant trend. This shows that the Arctic sea ice cover looses its capability to enhance the momentum flux into the ocean as it becomes thinner, younger and less deformed.

4. Discussion

4.1. Comparison to Previous Work

Our goal is to identify and quantify the impact of spatially and temporally varying sea ice surface roughness on momentum transfer into the Arctic Ocean and its changes related to current sea ice loss. In the following we discuss our results in light of the few studies known to us that have so far dealt with basin-wide estimates of either surface roughness or ocean surface stress.

Recently, *Castellani et al.* [2014] published sea ice roughness parameters and drag coefficients based on airborne laser altimeter measurements from 1995 to 2011 including profiles from various parts of the central and eastern Arctic Ocean including ice just north of the Laptev Sea, in the Transpolar Drift Stream, off Greenland, and also in the Beaufort Sea. Comparing our modeled sea ice roughness with these observations we find good agreement for thick ice north of Greenland where both observation-derived and modeled air-ice drag coefficients are around 2.6×10^{-3}. However, relatively young and thin ice in the central Arctic originating from, for instance, the Laptev Sea is much less rough in our simulations, $0.6–1.3 \times 10^{-3}$, compared to the observational values of about 1.6×10^{-3}. *Guest and Davidson* [1991] relate values below 1.0×10^{-3} only to grease ice and assign a range of $1.2–1.9 \times 10^{-3}$ to "smooth" first-year ice. They associate drag coefficients of 2×10^{-3} to 4×10^{-3} with "smooth" multiyear ice or any "rough" ice. The discrepancy between the model values and observations is largest for first-year ice in winter when the contribution from floe edges is negligible. The observations suggest that first year ice albeit thinner than multiyear ice can have a similar surface roughness to multiyear ice when being deformed, i.e., "rough," and that the parameterization in our model yields a too strong dependency of the surface roughness on ice thickness (cf. Figures 2b and 11c) and a too weak relationship to the state of deformation. This can be related to uncertainties in the ridging scheme of CICE [*Lipscomb et al.*, 2007], which computes the deformed ice volume applied to the parameterization of the ridge form drag coefficient.

Using the coupled sea ice-ocean model PIOMAS, which only considers a constant sea ice surface roughness, *Martin et al.* [2014] found that annual mean ocean surface stress increased over the period 1979–2012, a trend that is particularly strong in winter, but decreased over the last three decades in summer. They also suggested an ice concentration of 80–90% to be optimal for momentum transfer into the ocean based on their simulation (gray line in Figure 10a). While all our experiments support this optimal ice concentration only the simulation SKIN with constant drag coefficients agrees with the increase of annual mean ocean surface stress. The discrepancies to the experiments with variable drag during the winter season clearly relate to the trend in surface roughness, which the current version of PIOMAS cannot simulate. Interestingly, SKIN does not show a decrease in ocean surface stress for summer. This negative trend reported by *Martin et al.* [2014] depends on the contrast of the drag coefficients for sea ice and for open water. PIOMAS uses a constant sea ice surface roughness of 5×10^{-3}, which corresponds to a neutral air-ice drag coefficient of 2.8×10^{-3}, whereas a constant drag coefficient of 1.3×10^{-3} is used in SKIN, which is very close to the average open water drag coefficient of 1.2×10^{-3} derived from equation (3). Moreover, the difference in wind speed between the NCEP/NCAR and the NCEP-DOE-2 reanalyses discussed in section 2.2 causes the average ocean surface stress over open water to be 0.03 N/m^2 (43%) less in the PIOMAS simulation of *Martin et al.* [2014] than in our CICE experiments (Figure 10a). Consequently, the contrast between ocean surface stress in open water and surface stress at the optimal ice concentration of 80–90% is higher in PIOMAS than in the SKIN run (0.046 N/m^2 instead of 0.036 N/m^2, a factor of 3 instead of 1.7), which explains why the ice loss creates a significant decrease in ocean surface stress in summer in the PIOMAS simulation but not in our SKIN run.

Another aspect is that the ice interaction force is $0.01–0.02$ N/m^2 larger in PIOMAS than in the CICE simulations during summer and even twice as big in winter (in PIOMAS up to 0.08 N/m^2 in the 1980s, decreasing to 0.06 N/m^2 in 2012; for our CICE runs see Figure 4f). This significantly affects the trend in ocean surface stress. Note that in PIOMAS sea ice strength is parameterized according to *Hibler* [1979] but follows the

approach of *Flato and Hibler* [1995] in our simulation. While this by itself does not set the difference in basin-mean ice interaction force, it affects the spatial distribution because the latter is linked more closely to the ice deformation whereas the former is a function of ice thickness and concentration. The PIOMAS results support the notion of an optimal ice thickness for momentum transfer at 2–3 m (gray lines in Figures 11b and 11c). The linear dependency of ice strength on ice thickness in this model and its larger ice interaction force may explain the more pronounced peak.

4.2. Shortcomings

There are no basin-wide direct observations of the momentum flux into the Arctic Ocean and an estimation of the momentum flux and its trend is inhibited by lack of spatial and temporal coverage of measurements of ocean currents, surface roughness, and sea ice strength. We thus turn to numerical models to quantify the momentum flux and understand its seasonal and long-term changes. Such an approach is afflicted with uncertainty as knowledge is often incomplete and simplifications are made. First of all, we use a stand-alone sea ice model. To our knowledge this model is at the moment the only basin-scale model accounting for variable sea ice surface roughness [*Tsamados et al.*, 2014]. This model is forced with climatological ocean currents and thus lacks the feedback of an interactive ocean, which in turn could affect sea ice motion, surface roughness and the ocean surface stress. However, we are confident that our arguments hold qualitatively. Our control run SKIN with constant drag coefficients yields ocean surface stress magnitudes and trends (Figures 1a–1c) that agree remarkably well with the results of *Martin et al.* [2014] who used a coupled sea ice-ocean model. Further, the integrated ocean surface stress, i.e., the total momentum that would enter the Arctic Ocean over the year from SKIN and FORM, is also very similar to PIOMAS with 6.0×10^{21} and 5.7×10^{21} Ns compared to 5.4×10^{21} Ns for the first decade of the simulation before individual trends dominate. We thus argue that the uncertainty added by using a stand-alone sea ice model is not larger than the uncertainty associated with the sea ice-ocean momentum coupling scheme [*Martin and Gerdes*, 2007] and smaller than the impact of the processes discussed, such as variable surface roughness and ice strength.

Additional uncertainty that keeps us from exactly quantifying the momentum flux with the help of this model comes with the variable sea ice drag coefficient parameterizations. The parameters involved are either not well constrained by observations or have a broader distribution with unknown mean. *Tsamados et al.* [2014] show that the variability of the drag coefficients impacts the spatial distribution and variability of the ice thickness and drift velocity. Accordingly, the uncertainty associated with the choice of parameter settings in the sea ice roughness parameterizations is reflected by significant uncertainty for the total sea ice volume and basin-mean winter ice drift speed estimates. The authors went through a detailed testing procedure to suggest parameter settings that fit observations best and the present study uses these settings.

Similarly for the floe edge form drag coefficient we only model an average floe size, which we assume to scale non-linearly with sea ice concentration (equation (5)). Inherent to this approach is that the distance between floes is growing with decreasing floe size, which does not necessarily hold for floe aggregates in reality. However, it yields a good first guess of floe sizes as small as 10 m in the MIZ and up to 300 m in the pack ice, at which the contribution by floe edge form drag becomes negligible. This is in agreement with *Steele et al.* [1989], who mapped the parameter space of skin and form drag as functions of ice concentration (0–1) and floe size (5–1000 m). Yet, the model does not account for processes that actually determine floe sizes, such as breaking of floes by wind and waves, formation of floe clusters, and their refreezing to whole aggregates. In this respect more sophisticated floe size models are desirable as, for example, put forward by *Herman* [2012] and *Zhang et al.* [2015].

In this study our focus is on ocean surface stress as defined by equation (1) and we thus investigate the variability of the ice-water rather than the air-ice drag coefficient. Drag coefficients can also vary significantly depending on the stability of the atmosphere near the ice (and open water) surface as was shown for air-ice drag by, for instance, *Birnbaum and Lüpkes* [2002]. We derive form drag coefficients for the case of neutral stratification. Combined with the neutral skin drag coefficient to a total neutral air-ice drag coefficient (equation (A2)) the latter then is corrected by an atmospheric surface layer model, which accounts for the stability of this layer [*Briegleb et al.*, 2004], in our model and those used by *Tsamados et al.* [2014] and *Martin et al.* [2014]. This approach cannot replace a complex atmosphere model and we neglect feedbacks in the atmospheric boundary layer above 10 m height to the simulated surface roughness change. Only very recently similar surface layer model approaches for the ocean [e.g., *McPhee*, 2012] have been tested for the

first time in a basin-scale ice-ocean model by *Roy et al.* [2015] and are not yet accounted for here. Most recently as well, stability-dependent parameterizations of momentum and heat transfer coefficients over sea ice that explicitly account for form drag have been developed by *Lüpkes and Gryanik* [2015]. Interestingly, the authors note that depending on stability the maximum of the air drag coefficient can be found anywhere between 20 and 80% sea ice concentration. We expect a more accurate representation of the atmospheric (and oceanic) stability to influence the momentum transfer into the ocean directly on open water and through the sea ice cover. While stability-dependent parameterizations of the form drag coefficients for either the air-ice [*Lüpkes and Gryanik*, 2015] or the ice-water interface [*McPhee*, 2012] are beyond the scope of the present study, they deserve to be considered in future studies.

A process that is not resolved by most Arctic Ocean models is the formation of internal waves as a result of inertial motions triggered by the passing of storms. This shortcoming is likely related to either insufficient spatial and temporal resolution or lack of coupling between atmosphere, sea ice, and ocean. Internal waves transfer momentum into deeper layers of the ocean and trigger mixing processes. An increase in the formation of inertial internal waves in the Arctic Ocean has largely been associated with the complete retreat of sea ice from the observation site [*Rainville and Woodgate*, 2009] but there is also some indication of a loose ice cover being optimal to enhance internal wave energy based on recent mooring and ice tethered profiler observations [*Martini et al.*, 2014; *Dosser and Rainville*, 2016]. Including such processes that demand high-resolution coupled models also is beyond the scope of our experiments.

5. Conclusions

The impact of variable sea ice surface roughness on Arctic Ocean surface stress is studied with a version of the sea ice model CICE that features variable air-ice and ice-water drag coefficients as functions of derived ridge, floe, and melt pond statistics [*Tsamados et al.*, 2014]. A control simulation with constant drag coefficients demonstrates the suitability of the stand-alone model for investigations of the ocean surface stress and yields a clean reference for studying the impact of the variable drag coefficients. Five simulations with variable drag coefficients are then used to study the impact of changing sea ice roughness and strength on ocean surface stress.

The reference experiment with constant neutral air-ice and ice-water drag coefficients shows an overall *increase* in Arctic Ocean surface stress of 0.003 N/m^2 per decade from 1980 to 2013. The trend is linked to the reduction in sea ice thickness and strength and most pronounced during the winter season. In contrast, annual mean ocean surface stress is *decreasing* at −0.002 N/m^2 per decade in the baseline experiment with variable drag coefficients. These coefficients are closely related to sea ice thickness and the amount of deformed ice. Consequently, sea ice thinning and extensive loss of ridged ice since the 1980s reduced the surface roughness of the Arctic sea ice cover but also its strength. While the former causes less momentum to be transferred into the ocean the latter allows a larger momentum flux and the actual trend in ocean surface stress depends on the balance between surface roughness and ice strength. Accordingly, the negative ocean surface stress trend is reduced (−0.001 N/m^2 per decade for 1980–2013) with a weak increase after 2000 (0.001 N/m^2 per decade) in another experiment with stronger ice. Note, our experiments demonstrate the sensitivity of the system but further observational support is needed for an exact estimate of the balance of forces.

In summer the sea ice cover is less compact and the internal ice stress within the ice pack becomes small compared to the other forces—the ice is in free drift, which makes it most effective for momentum transfer. For all our simulations we find ocean surface stress to be maximal at an optimal ice concentration of 80–90%. Its relevance, however, depends on the contrast between sea ice and open water surface roughness and hence also on the wind product used to force the model, as well as atmospheric and oceanic boundary layer stability.

In our simulations with variable sea ice roughness, the presence of ice does not always amplify the momentum flux. For example, the drag coefficient of newly formed ice in fall is smaller than the one computed for open water and thus a compact young undeformed sea ice cover rather damps the momentum flux. In simulations with constant drag coefficient only the ice interaction force can limit the capability of sea ice to transfer momentum. Therefore, ocean surface stress decreases over the winter season in such simulations as ice grows thicker and stronger but not in the ones with variable drag where the ice also becomes rougher. Further, at mid to low sea ice concentrations, which are characteristic for the marginal sea ice zone

but have become typical also for the central Arctic pack ice during summers of the last decade, form drag by floe edges dominates the total ice-water drag coefficient. This causes the seasonal cycle of ocean surface stress to peak in August, 2 months earlier than in simulations with constant neutral drag coefficients, and the average surface stress is higher in summer than in winter. Nevertheless, the summer trend for the basin-mean surface stress is still negative in the simulations with variable floe edge form drag, a result of the increase in open water area.

In simulations with global climate models, sea ice roughness is typically set to a constant value, which usually prescribes a larger surface roughness for sea ice than simulated for open water. Our study shows that such models lack a complete representation of feedbacks between sea ice thickness, drift, surface roughness, strength, deformation, and momentum transfer. The simulations cannot reflect the full potential of the ice cover to moderate the momentum flux into the ocean, which has changed over the past three decades. In order to fully understand changes of the coupling between atmosphere, sea ice, and ocean dynamics further improvements in observational coverage of sea ice thickness, ice strength, and surface roughness as well as model techniques are needed. Such improved understanding of, and ability to model, the air to ocean momentum transfer in the presence of sea ice will become increasingly significant as the Arctic transitions into a seasonal sea ice regime under global warming.

Appendix A

In presence of sea ice, the direct air-sea momentum flux is interrupted and momentum is exchanged through the ice by fluxes at the air-ice and ice-water interface. A common and intuitive approach to compute exchange fluxes in models of ice-covered seas is applying a linear mixture relationship, i.e., the total flux is the sum of the fluxes of the individual surface types weighted by their fractional area. This yields three cases of momentum transfer to be computed as individual surface stresses. While a sea ice model such as the one used in the present study is forced by the air-ice (τ_{ai}) and ice-water fluxes (τ_{iw}), an ocean model would receive the open water (τ_{ao}) and ice-water stresses (equation (1)) with the latter pointing the opposite direction as in the sea ice momentum balance ($-\tau_{iw}$, cf. equation (2b)). All three surface (or interface) stresses are typically computed using a quadratic drag law (cf. equation (2)):

$$\vec{\tau}_{ao} = \rho_a C_{dao} |\vec{u}_a| \vec{u}_a \tag{A1a}$$

$$\vec{\tau}_{ai} = \rho_a C_{da} |\vec{u}_a| \vec{u}_a \tag{A1b}$$

$$\vec{\tau}_{iw} = \rho_w C_{dw} |\vec{u}_w - \vec{u}_i| (\vec{u}_w - \vec{u}_i) \tag{A1c}$$

with ρ_a and ρ_w the density of air and water, respectively, C_{dao} and C_{da} the total atmospheric drag coefficients over open water and ice, C_{dw} the total ice-water drag coefficient, and $\boldsymbol{u}_a$, $\boldsymbol{u}_w$, and $\boldsymbol{u}_i$ the velocities of (near) surface wind, currents and ice drift. In equations (A1a) and (A1b) the ocean current and ice drift velocities are neglected assuming they are small relative to the wind speed (cf. equation (2a)). The open water atmospheric drag coefficient is parameterized as a function of wind speed (see equation (3)).

In our model the total neutral air-ice drag coefficient is the sum of the neutral skin drag coefficient (C_{da_skin}) and neutral form drag coefficients for ridges (C_{da_ridge}), floe edges (C_{da_floe}) and melt pond edge (C_{da_pond})

$$C_{da} = C_{da\_skin} + C_{da\_ridge} + C_{da\_floe} + C_{da\_pond} \tag{A2}$$

which as a whole is corrected for the stability of the atmospheric surface layer following the approach of *Briegleb et al.* [2004] before being applied to the surface stress balance (equation (A1b)). Similarly, the total ice-water drag coefficient at the ice underside is composed of neutral skin (C_{dw_skin}) and form drag coefficients with the latter only accounting for ridge keels (C_{dw_ridge}) and floes edges (C_{dw_floe})

$$C_{dw} = C_{dw\_skin} + C_{dw\_ridge} + C_{dw\_floe} \tag{A3}$$

Here potential effects of the oceanic stratification are not accounted for, however, and the drag coefficient is applied to the undisturbed ocean currents relative to the ice drift in equation (A1c).

In the following we provide a brief overview of the quantities playing a role in computing the variable neutral drag coefficients. The details of the underlying theory and specific parameter settings including sensitivity tests are presented in *Tsamados et al.* [2014]; the same model is used here. In principle, the definition of

the drag force of an obstacle oriented normal to the mean floe [*Arya*, 1973] is scaled to be applicable to a number of such obstacles distributed evenly over a defined surface area. The approach follows *Lüpkes et al.* [2012] in defining the average dynamic pressure per obstacle including a sheltering function, which reduces the drag for densely packed obstacles, and a geometric shape function, which introduces a uniform distribution for the obstacle orientation to the mean flow. Finally, a logarithmic fluid velocity profile is assumed to bridge the gap between the flow at a certain height (or depth), for instance 10 m, and the surface drag.

Based on these assumptions, the equations for form drag from ridges and floe edges at both the air-ice and ice-water interface and the form drag from melt pond edges at the air-ice interface all follow the same scheme: (1) the form drag only applies to the ice covered area fraction of the grid cell, (2) a constant local form drag coefficient c prescribes the base magnitude, (3) a sheltering effect is accounted for by S_c, which depends on the height H and distance D between obstacles, and (4) the roughness length of the obstacle-free surface z_0. The form drag caused by ridges is parameterized as

$$C_{dx\_ridge} = A_i \frac{1}{2} c_{rx} S_c 2 \frac{H_y}{D_y} \left[\frac{\ln(H_y/z_{0i})}{\ln(10/z_{0i})} \right]^2 \tag{A4}$$

with indices $x = [a,w]$ and $y = [s,k]$ referring to the air-ice (a) and ice-water (w) interfaces with height (or depth) H and distance D between ridge sails (s) and keels (k), respectively. The local form drag coefficients are $c_{ra} = 0.2$ and $c_{rw} = 0.2$, z_{0i} is the roughness length of level ice (5×10^{-4} m) [*Hunke et al.*, 2013]. As described in more detail in *Tsamados et al.* [2014] the ridge statistics H_s and D_s are derived from the deformed ice volume resulting from the ridging scheme in CICE [*Lipscomb et al.*, 2007].

Similarly, form drag by floe edges is given by

$$C_{dx\_floe} = A_i \frac{1}{2} \frac{c_{fx}}{c_{sf}} S_c 2 \frac{H_y}{L_f} \left[\frac{\ln(H_y/z_{0w})}{\ln(10/z_{0w})} \right]^2 \tag{A5}$$

considering a floe freeboard (or draft) H depending on the actual ice thickness and a floe diameter L_f, which is parameterized as a function of ice concentration (see equation (5)). Here $c_{fa} = 0.2$ and $c_{fw} = 0.2$, and c_{sf} is a floe shape parameter ($\pi/4$ for circular, 1 for square floes) set to 0.2, and z_{0w} the roughness length of water upstream of the obstacle (3.27×10^{-4} m) [*Hunke et al.*, 2013].

Form drag by melt pond edges only affects momentum transfer at the air-ice interface and is parameterized by

$$C_{da\_pond} = A_i \frac{1}{2} \frac{c_{pa}}{c_{sp}} S_c 2 \frac{H_p}{L_p} A_p \left[\frac{\ln(H_p/z_{0w})}{\ln(10/z_{0w})} \right]^2 \tag{A6}$$

comprising the pond geometry $c_{sp} = 0.2$, the pond edge height H_p, pond length L_p, and the ponded ice area fraction A_p. The local form drag coefficient for ponds c_{pa} is set to 0.2.

The skin drag coefficient is set by a constant unobstructed skin drag c_{sx} and potentially modified by the presence of ridges

$$C_{dx\_skin} = A_i c_{sx} \left(1 - m_x \frac{H_y}{D_y} \right) , \quad \text{if} \quad \frac{H_y}{D_y} \leq \frac{1}{m_x} \tag{A7}$$

with indices $x = [a,w]$ and $y = [s,k]$ referring to the air-ice (a) and ice-water (w) interfaces with ridge sails (s) and keels (k), respectively. For our experiments, we chose the unobstructed skin drag c_{sx} to equal 5×10^{-4} for the air-ice interface (c_{sa}) and 20×10^{-4} for the ice-water interface (c_{sw}), and parameters m_a and m_w were given the values 20 and 10, respectively. The sheltering effect thus depends on either the sail height H_s or the keel depth H_k and their respective frequency of occurrence of sails D_s and keels D_k.

Lastly, we would like to add a cautionary note: When applying the linear mixture relationship for different surface types it is obvious for the ocean model that the two surface stresses are weighed by the fractional ice-covered (A_i) and open water areas ($1-A_i$) (equation (1)) but less so for a sea ice model. *Connolley et al.* [2004] showed, however, that the ice concentration factor also needs to be applied to the surface stresses in the sea ice momentum balance. Confusion may arise from the sea ice concentration A_i being a factor in the equations above defining the various drag coefficients (equations (A4)–(A7)) and the one determining

the total ocean surface stress (equation (1)). Since in both cases the factor originates from the linear mixture relationship, it must be considered only once in either the drag coefficient or surface stress relationship in the model code.

References

Andreas, E. L., T. W. Horst, A. A. Grachev, P. O. G. Persson, C. W. Fairall, P. S. Guest, and R. E. Jordan (2010), Parametrizing turbulent exchange over summer sea ice and the marginal ice zone, *Q. J. R. Meteorol. Soc.*, *136*(649), 927–943, doi:10.1002/qj.618.

Arya, S. (1973), Contribution of form drag on pressure ridges to the air stress on Arctic ice, *J. Geophys. Res.*, *78*(30), 7092–7099, doi:10.1029/JC078i030p07092.

Birnbaum, G., and C. Lüpkes (2002), A new parameterization of surface drag in the marginal sea ice zone, *Tellus, Ser. A*, *54*, 107–123.

Briegleb, B. P., C. M. Bitz, E. C. Hunke, W. H. Lipscomb, M. M. Holland, J. L. Schramm, and R. E. Moritz (2004), Scientific description of the sea ice component in the community climate model, version 3, *Tech. Note NCAR/TN-4631STR*, 78 pp., Natl. Cent. for Atmos. Res., Boulder, Colo.

Castellani, G., C. Lüpkes, S. Hendricks, and R. Gerdes (2014), Variability of Arctic sea-ice topography and its impact on the atmospheric surface drag, *J. Geophys. Res. Oceans*, *119*, 6743–6762, doi:10.1002/2013JC009712.

Cavalieri, D. J., and C. L. Parkinson (2012), Arctic sea ice variability and trends, 1979–2010, *Cryosphere*, *6*(4), 881–889, doi:10.5194/tc-6-881-2012.

Cole, S. T., M.-L. Timmermans, J. M. Toole, R. A. Krishfield, and F. T. Thwaites (2014), Ekman veering, internal waves, and turbulence observed under Arctic Sea Ice, *J. Phys. Oceanogr.*, *44*(5), 1306–1328, doi:10.1175/JPO-D-12-0191.1.

Connolley, W. M., J. M. Gregory, E. Hunke, and A. J. McLaren (2004), On the consistent scaling of terms in the sea-ice dynamics equation, *J. Phys. Oceanogr.*, *34*(7), 1776–1780.

Dosser, H. V., and L. Rainville (2016), Dynamics of the changing near-inertial internal wave field in the Arctic Ocean, *J. Phys. Oceanogr.*, *46*, 395–415, doi: 10.1175/JPO-D-15-0056.1.

Ferry, N., S. Masina, A. Storto, K. Haines, B. Valdivieso, B. Barnier, and J.-M. Molines (2011), Product User Manual, GLOBAL-REANALYSIS-PHYS-001-004-a and b, 30 pp., MyOcean, Eur. Comm., Brussels.

Flato, G. M., and W. D. Hibler (1995), Ridging and strength in modeling the thickness distribution of Arctic Sea-Ice, *J. Geophys. Res.*, *100*(C9), 18,611–18,626.

Giles, K. A., S. W. Laxon, A. L. Ridout, D. J. Wingham, and S. Bacon (2012), Western Arctic Ocean freshwater storage increased by wind-driven spin-up of the Beaufort Gyre, *Nat. Geosci.*, *5*, 194–197, doi:10.1038/ngeo1379.

Guest, P. S., and K. L. Davidson (1991), The aerodynamic roughness of different types of sea ice, *J. Geophys. Res.*, *96*(C3), 4709–4721.

Herman, A. (2012), Influence of ice concentration and floe-size distribution on cluster formation in sea-ice floes, *Open Phys.*, *10*(3), 715–722, doi:10.2478/s11534-012-0071-6.

Hibler, W. D. (1979), A dynamic thermodynamic sea ice model, *J. Phys. Oceanogr.*, *9*, 815–846.

Hopkins, M. A. (1994), On the ridging of intact lead ice, *J. Geophys. Res.*, *99*(C8), 16,351–16,360.

Hunke, E. C., W. H. Lipscomb, A. K. Turner, N. Jeffery, and S. Elliott (2013), CICE: The Los Alamos Sea Ice Model Documentation and Software User's Manual Version 5.0, *Tech. Rep. LA-CC-06-012*, Los Alamos Natl. Lab., Los Alamos, N. M.

Kanamitsu, M., W. Ebisuzaki, J. Woollen, S.-K. Yang, J. J. Hnilo, M. Fiorino, and G. L. Potter (2002), NCEP–DOE AMIP-II Reanalysis (R-2), *Bull. Am. Meteorol. Soc.*, *83*(11), 1631–1643, doi:10.1175/BAMS-83-11-1631.

Kwok, R., G. Spreen, and S. Pang (2013), Arctic sea ice circulation and drift speed: Decadal trends and ocean currents, *J. Geophys. Res. Oceans*, *118*, 2408–2425, doi:10.1002/jgrc.20191.

Large, W. G., and S. Pond (1981), Open ocean momentum flux measurements in moderate to strong winds, *J. Phys. Oceanogr.*, *11*(3), 324–336.

Lindsay, R., and A. Schweiger (2015), Arctic sea ice thickness loss determined using subsurface, aircraft, and satellite observations, *Cryosphere*, *9*, 269–283, doi:10.5194/tc-9-269-2015.

Lindsay, R., M. Wensnahan, A. Schweiger, and J. Zhang (2014), Evaluation of Seven Different Atmospheric Reanalysis Products in the Arctic*, *J. Clim.*, *27*(7), 2588–2606, doi:10.1175/JCLI-D-13.

Lipscomb, W. H., E. C. Hunke, W. Maslowski, and J. Jakacki (2007), Ridging, strength, and stability in high-resolution sea ice models, *J. Geophys. Res.*, *112*, C03S91, doi:10.1029/2005JC003355.

Lüpkes, C., and V. M. Gryanik (2015), A stability-dependent parametrization of transfer coefficients for momentum and heat over polar sea ice to be used in climate models, *J. Geophys. Res. Atmos.*, *120*, 552–581, doi:10.1002/2014JD022418.

Lüpkes, C., V. M. Gryanik, J. Hartmann, and E. L. Andreas (2012), A parametrization, based on sea ice morphology, of the neutral atmospheric drag coefficients for weather prediction and climate models, *J. Geophys. Res.*, *117*, D13112, doi:10.1029/2012JD017630.

Martin, T. (2007), Arctic Sea Ice Dynamics: Drift and ridging in numerical models and observations, *Ber. zur Polar Meeresforsch.*, *563*, 229.

Martin, T., and R. Gerdes (2007), Sea ice drift variability in Arctic Ocean Model Intercomparison Project models and observations, *J. Geophys. Res.*, *112*, C04S10, doi:10.1029/2006JC003617.

Martin, T., M. Steele, and J. Zhang (2014), Seasonality and long-term trend of Arctic Ocean surface stress in a model, *J. Geophys. Res. Oceans*, *119*, 1723–1738, doi:10.1002/2013JC009425.

Martini, K. I., H. L. Simmons, C. A. Stoudt, and J. K. Hutchings (2014), Near-inertial internal waves and sea ice in the Beaufort Sea*, *J. Phys. Oceanogr.*, *44*(8), 2212–2234, doi:10.1175/JPO-D-13-0160.1.

Maslanik, J., J. Stroeve, C. Fowler, and W. Emery (2011), Distribution and trends in Arctic sea ice age through spring 2011, *Geophys. Res. Lett.*, *38*, L13502, doi:10.1029/2011GL047735.

McPhee, M. G. (2012), Advances in understanding ice–ocean stress during and since AIDJEX, *Cold Reg. Sci. Technol.*, *76*, 24–36, doi:10.1016/j.coldregions.2011.05.001.

McPhee, M. G. (2013), Intensification of geostrophic currents in the Canada Basin, Arctic Ocean, *J. Clim.*, *26*(10), 3130–3138, doi:10.1175/JCLI-D-12-00289.1.

McPhee, M. G., A. Proshutinsky, J. H. Morison, M. Steele, and M. B. Alkire (2009), Rapid change in freshwater content of the Arctic Ocean, *Geophys. Res. Lett.*, *36*, L10602, doi:10.1029/2009GL037525.

Rabe, B., M. Karcher, U. Schauer, J. M. Toole, R. A. Krishfield, S. Pisarev, F. Kauker, R. Gerdes, and T. Kikuchi (2011), Deep-sea research I, *Deep Sea Res., Part I*, *58*(2), 173–185, doi:10.1016/j.dsr.2010.12.002.

Rainville, L., and R. A. Woodgate (2009), Observations of internal wave generation in the seasonally ice-free Arctic, *Geophys. Res. Lett.*, *36*, L23604, doi:10.1029/2009GL041291.

Roy, F., M. Chevallier, G. C. Smith, F. Dupont, G. Garric, J.-F. Lemieux, Y. Lu, and F. Davidson (2015), Arctic sea ice and freshwater sensitivity to the treatment of the atmosphere-ice-ocean surface layer, *J. Geophys. Res. Oceans*, *120*, 4392–4417, doi:10.1002/2014JC010677.

Steele, M., J. H. Morison, and N. Untersteiner (1989), The partition of air-ice-ocean momentum exchange as a function of ice concentration, floe size, and draft, *J. Geophys. Res.*, *94*(C9), 12,739–12,750, doi:10.1029/JC094iC09p12739.

Steele, M., J. Zhang, D. Rothrock, and H. Stern (1997), The force balance of sea ice in a numerical model of the Arctic Ocean, *J. Geophys. Res.*, *102*(C9), 21,061–21,079.

Steiner, N., M. Harder, and P. Lemke (1999), Sea-ice roughness and drag coefficients in a dynamic–thermodynamic sea-ice model for the Arctic, *Tellus, Ser. A*, *51*(5), 964–978.

Tremblay, L. B., and L. A. Mysak (1997), The possible effects of including ridge-related roughness in air-ice drag pararneterization: A sensitivity study, *Ann. Glaciol.*, *25*, 22–25.

Tsamados, M., D. L. Feltham, D. Schroeder, D. Flocco, S. L. Farrell, N. Kurtz, S. W. Laxon, and S. Bacon (2014), Impact of variable atmospheric and oceanic form drag on simulations of Arctic Sea Ice*, *J. Phys. Oceanogr.*, *44*(5), 1329–1353, doi:10.1175/JPO-D-13-0215.1.

Tsamados, M., D. Feltham, and A. Petty (2015), Processes controlling surface, bottom and lateral melt of Arctic sea ice in a state of the art sea ice model, *Philos. Trans. R. Soc. A*, *373*(2052), doi:10.1098/rsta.2014.0167.

Yang, J. (2009), Seasonal and interannual variability of downwelling in the Beaufort Sea, *J. Geophys. Res.*, *114*, C00A14, doi:10.1029/2008JC005084.

Zhang, J., A. Schweiger, M. Steele, and H. Stern (2015), Sea ice floe size distribution in the marginal ice zone: Theory and numerical experiments, *J. Geophys. Res. Oceans*, *120*, 3484–3498, doi:10.1002/2015JC010770.